International Journal for Numerical Methods in Fluids

WILEY

RESEARCH ARTICLE OPEN ACCESS

Monolithic Framework to Simulate Fluid-Structure Interaction Problems Using Geometric Volume-of-Fluid Method

Soham Prajapati[1] | Ali Fakhreddine[1] | Krishnan Mahesh[2,3,4]

[1]Department of Aerospace Engineering and Mechanics, University of Minnesota—Twin Cities, Minneapolis, Minnesota, USA | [2]Department of Naval Architecture and Marine Engineering, University of Michigan, Ann Arbor, Michigan, USA | [3]Department of Mechanical Engineering, University of Michigan, Ann Arbor, Michigan, USA | [4]Department of Aerospace Engineering, University of Michigan, Ann Arbor, Michigan, USA

Correspondence: Krishnan Mahesh (krmahesh@umich.edu)

Received: 2 May 2025 | **Revised:** 19 December 2025 | **Accepted:** 7 May 2026

Keywords: fluid-structure interaction | geometric VOF | turbulent flows

ABSTRACT

We develop a three-dimensional Eulerian framework to simulate fluid-structure interaction (FSI) problems on a fixed Cartesian grid using the geometric volume-of-fluid (VOF) method. The coupled problem involves incompressible flow and viscous hyperelastic solids. A VOF-based one-continuum formulation is used to describe the unified momentum conservation equations with incompressibility constraints that are solved using the finite volume method (FVM). In the geometric VOF interface-capturing (IC) approach, the piecewise linear interface calculation (PLIC) method is used to reconstruct the interface, and the Lagrangian explicit (LE) method is used in the directionally split advection procedure. To model the hyperelastic behavior of the solid, we consider linear and nonlinear Mooney–Rivlin material models, where we use the left Cauchy–Green deformation tensor ($\boldsymbol{B}$) to account for the solid deformation on an Eulerian grid and the fifth-order weighted essentially non-oscillatory (WENO-Z) finite difference reconstruction method is utilized to treat the advection terms involved in the transport equation of $\boldsymbol{B}$. Multiple benchmark problems and reversibility tests are considered to verify the accuracy of the approach. Furthermore, to demonstrate the capability of the solver to handle turbulent interactions, we perform direct numerical simulation (DNS) of turbulent channel flow with a deformable compliant bottom wall and a rigid top wall; our observations align well with previous experimental and numerical works. The detailed numerical experiments show that: (i) despite the discontinuity of the interface across the cell boundaries and stress discontinuity across the interface, a VOF/PLIC-based FSI framework can provide stable and accurate solutions that significantly minimizes numerical artifacts (e.g., flotsam and spurious currents) while maintaining a sharp interface. (ii) The accuracy of a VOF/PLIC-based FSI approach on coarse grids is comparable to the accuracy of a diffusive IC method-based FSI approach on much finer grids.

1 | Introduction

The dynamic interaction of fluid flows with deformable structures is crucial in various sectors, such as the marine, healthcare, and aerospace industries. Accurately modeling such fluid-structure interaction (FSI) problems enables us to perform detailed assessments of complex processes such as the interaction of deformable compliant coatings with turbulent flows

[1–4], the impact of marine biofouling on the turbulent flowfield near the affected surfaces [5–7], and the rheology of red blood cells [8–11].

Most of the mesh-based numerical methods used to model FSI problems can be broadly classified into three categories [12]: (i) fully Eulerian methods, where the Eulerian grid represents both subsystems, (ii) mixed Lagrangian–Eulerian methods, where mostly Lagrangian and Eulerian grids represent solid and fluid subsystems, respectively, and (iii) fully Lagrangian methods, where the Lagrangian grid represents both subsystems. For a brief overview of the different types of FSI approaches, we refer the readers to Jain et al. [12]. The mixed Lagrangian–Eulerian methods can be further classified into two categories: (i) partitioned approach, where both systems are solved separately, and (ii) monolithic approach, where both systems are solved simultaneously. The partitioned mixed Lagrangian–Eulerian methods such as arbitrary Lagrangian–Eulerian (ALE) [13–16] and deforming-spatial-domain/stabilized-space-time (DSD/SST) [17–19] procedures are extensively adopted to simulate a variety of FSI problems such as blood flow [20–23], parachute modeling [24, 25], and flapping wings [26, 27]. However, such partitioned approaches can become expensive for large deformations due to grid reconstruction requirements. To address the computational cost issue, monolithic approaches such as immersed boundary (IB) [28–30], fictitious domain (FD) [31–33], immersed finite-element [34, 35], immersed interface [36, 37], and immersed continuum [38] methods were developed. These methods are utilized to simulate a wide range of FSI problems, such as red blood cell dynamics [39, 40], flexible plate vibration [33, 41, 42], and biofouling surface effects [5].

The fully Eulerian methods perform computations on a fixed Eulerian grid and generally utilize an interface capturing (IC) procedure to track the fluid–solid (FS) interface, similar to multiphase flows. These methods are cost-effective for the following reasons: (i) they do not require complex grid generation procedures, (ii) they can leverage the existing frameworks of fluid solvers, and (iii) they have the potential to scale well for large-scale problems. Over the years, multiple IC methods [43] have been developed to perform multiphase simulations. Some of the well-known approaches are the volume-of-fluid (VOF) method [44], level-set (LS) method [45], and phase-field (PF) method [46]. These methods are increasingly used to analyze FSI problems such as modeling red-blood cells [9–11], modeling blood vessel [47], examining droplet impact on flexible cantilever [48], and interaction of compliant coatings with turbulent flows [2–4]. These methods have their benefits and limitations. On one hand, VOF methods are well-known for their potential to conserve mass. However, for sharp IC methods like geometric VOF, interface normal estimation is not a straightforward task due to the discontinuous nature of the volume fraction. On the other hand, LS methods can estimate the interface normal more accurately due to the smoothness and differentiability of the LS function. However, LS methods do not inherently conserve mass and, in most cases, requires a reinitialization procedure that is problem-dependent and computationally costly.

Recently, FSI simulations involving incompressible flows and hyperelastic solids have been performed using the Eulerian method. Sugiyama et al. [49] used a fifth-order weighted essentially non-oscillatory (WENO) scheme [50] to treat the advection terms involved in the transport equations of the volume fraction and the left Cauchy–Green deformation tensor, Ii et al. [9] used MTHINC (multi-dimensional tangent of hyperbola for IC) method [51–53] to simulate red blood cells, and Esmailzadeh and Passandideh-Fard [54] used the piecewise linear interface calculation (PLIC) method to capture interface in 2D problems. Unlike Lagrangian approaches where mesh movement represents solid deformation, the Eulerian approach generally uses deformation tensors to account for solid displacements. Recently, a reference map technique (RMT) [12, 55] was introduced that utilizes a reference-map vector field to track solid deformation and was used to simulate the collision of elastic solids with rigid walls [12].

To analyze fully coupled problems involving turbulent flows, the two-way coupled FSI approach needs to be robust enough to tackle complex interactions that occur on a wide range of length scales and time scales, and the solver needs to scale well with the problem size. To perform a detailed analysis of the involved coupling, sometimes a simplistic one-way coupled FSI approach provides valuable insights. For example, Prajapati et al. [56] investigated the vibroacoustic response of elastic plates excited by turbulent flows and proposed new scaling laws, and Anantharamu and Mahesh [57] analyzed the sources of elastic plate vibrations excited by turbulent flows. However, such simplistic approaches are limited to a range of problem parameters because the dynamic coupling is assumed to be negligible. Recently, Eulerian methods have shown good potential to handle fully coupled large-scale problems such as the interaction of turbulent flows with deformable compliant coatings [2–4], where Esteghamatian et al. [2] used LS method to capture the fluid–solid interface, and Rosti and Brandt [3] used the VOF formulation and employed a fifth-order WENO scheme to treat the advection terms involved in the transport equations.

Geometric VOF methods [44, 58–63] are well-known procedures that use geometric representations to capture the interface. Two primary advantages of these methods are: (i) they maintain a sharp interface while avoiding interface diffusion, and (ii) they have the potential to achieve mass conservation to machine precision [60, 62, 63], depending on the numerical procedure. These methods involve two fundamental steps: reconstruction and advection. In the reconstruction step, interface shape and location in each computational cell are estimated, and in the advection step, the volume fractions across the cell boundaries are exchanged using the velocity field. One of the well-known reconstruction procedures is the PLIC [64–67] method that uses the neighboring cells to construct a piecewise linear interface. In the advection step, the volume fraction can be exchanged across cell boundaries using unsplit or directionally split methods. The unsplit geometric VOF methods allow the advection procedure in a single step, however, it involves implementing complex algorithms and has difficulties conserving mass. The split geometric VOF methods, on the other hand, perform the advection procedure in multiple steps, however, the numerics involved are relatively less complicated than the unsplit methods and have a high potential to conserve mass.

The geometric VOF method has many attractive features that make it suitable for 3D complex and turbulent FSI problems

involving a wide range of length scales and time scales. However, to the best of our knowledge, such a 3D FSI algorithm involving VOF/PLIC (geometric VOF using PLIC technique) method has not been developed yet. As a result, their potential to investigate such problems remains unexplored.

Designing a robust 3D FSI algorithm involving the VOF/PLIC method is not trivial because the discontinuity of the interface across the cell boundaries and discontinuities across the sharp interface can lead to numerical artifacts such as (i) nonphysical occurrence of solid fragments (flotsam) due to inappropriate numerical discretization and treatment of stress contributions, and (ii) unwanted surface oscillations (especially at equilibrium states) generated due to strong unphysical parasitic currents caused by an imbalance and jumps in the stress distribution across the sharp interface. Furthermore, a 3D interface reconstruction procedure is much more complex than a 2D procedure. This paper develops a 3D Eulerian framework that leverages the benefits of the VOF/PLIC method while avoiding any numerical artifacts typically associated with it.

In this work, we develop a three-dimensional monolithic FSI framework to simulate the interaction of incompressible flow and viscous hyperelastic solids on a fixed Cartesian grid. We use the geometric VOF method to capture the fluid–solid interface, where the PLIC method is used to reconstruct the interface and Lagrangian explicit (LE) [58, 61, 68] directionally split advection procedure is used to exchange the volume fraction across cell boundaries. Both linear and nonlinear Mooney–Rivlin hyperelastic material models are considered to capture the mechanical behavior of solids, where the left Cauchy–Green deformation tensor ($\boldsymbol{B}$) is used to account for the solid deformation on an Eulerian grid. To treat the advection terms involved in the transport of $\boldsymbol{B}$ tensor, we use the fifth-order WENO-Z [50, 69] finite difference reconstruction procedure, and to solve the unified momentum conservation equations with incompressibility constraints, we use the finite volume method (FVM) [70]. The procedure is designed to efficiently handle large-scale turbulent FSI problems involving a wide range of time scales and length scales. We thoroughly test the accuracy and robustness of the FSI algorithm using a variety of benchmark problems.

In Section 2, we discuss the methodology, where Section 2.1 presents the governing equations and Section 2.2 provides the numerical details. In Section 3, we discuss the numerical experiments. Finally, we conclude the paper in Section 4.

2 | Methodology

2.1 | Governing Equations

We consider the interaction of fluid and solid systems as shown in Figure 1. It shows the combined fluid–solid domain (Ω), where Ω^f is the fluid subdomain, Ω^s is the solid subdomain, and Γ_{fs} is the fluid–solid interface.

We solve the momentum conservation equation with an incompressibility constraint in both subdomains, that is, in the fluid

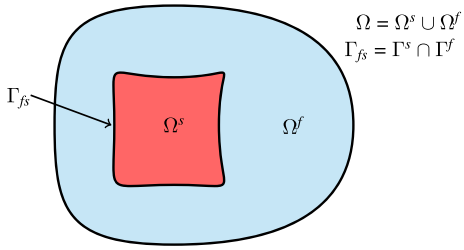

FIGURE 1 | Schematic of the problem. [Colour figure can be viewed at wileyonlinelibrary.com]

subdomain (Ω^f), the governing equations are

$$\frac{\partial u_i^f}{\partial t} + \frac{\partial u_i^f u_j^f}{\partial x_j} = -\frac{1}{\rho^f}\frac{\partial p^f}{\partial x_i} + \frac{1}{\rho^f}\frac{\partial \sigma_{ij}^f}{\partial x_j}, \frac{\partial u_i^f}{\partial x_i} = 0, \tag{1}$$

and in the solid subdomain (Ω^s),

$$\frac{\partial u_i^s}{\partial t} + \frac{\partial u_i^s u_j^s}{\partial x_j} = -\frac{1}{\rho^s}\frac{\partial p^s}{\partial x_i} + \frac{1}{\rho^s}\frac{\partial \sigma_{ij}^s}{\partial x_j}, \frac{\partial u_i^s}{\partial x_i} = 0, \tag{2}$$

where ρ is density, p is pressure, u_i is the velocity component, and σ_{ij} is a component of the stress tensor $\boldsymbol{\sigma}$. The subscripts $i = 1$, 2, and 3 correspond to x, y, and z directions, respectively. Superscripts f and s refer to fluid and solid quantities, respectively.

At the fluid–solid interface (Γ_{fs}), the kinematic and dynamic interaction requires continuity of velocity and traction force,

$$u_i^f = u_i^s, \tag{3}$$

$$\sigma_{ij}^f n_j = \sigma_{ij}^s n_j, \tag{4}$$

where n_j is the unit normal vector at Γ_{fs}.

The fluid–solid interface is implicitly tracked in the Eulerian frame of reference using a volume fraction ϕ, also known as the color function in VOF. By definition, $\phi = 0$ in the fluid domain, $\phi = 1$ in the solid domain, and $\phi \in (0, 1)$ at the fluid–solid interface. Details of the VOF methodology will be discussed in Section 2.2.2.

To solve the governing equations simultaneously, we use the one-continuum formulation [71], where monolithic quantities are defined over the whole domain ($\Omega = \Omega^f \cup \Omega^s$). We use a volume-averaging technique to define the monolithic velocity (u_i) as

$$u_i = \phi u_i^s + (1 - \phi) u_i^f, \tag{5}$$

and it inherently satisfies the kinematic interaction condition (3) at the fluid–solid interface. The unified representation of the governing Equations (1) and (2) is

$$\frac{\partial u_i}{\partial t} + \frac{\partial u_i u_j}{\partial x_j} = -\frac{1}{\rho}\frac{\partial p}{\partial x_i} + \frac{1}{\rho}\frac{\partial \sigma_{ij}}{\partial x_j}, \quad \frac{\partial u_i}{\partial x_i} = 0, \tag{6}$$

where ρ, p, and σ_{ij} are defined over the whole domain. The density and stress distribution over the entire domain are defined as

$$\rho = \phi\rho^s + (1-\phi)\rho^f, \tag{7}$$

$$\sigma_{ij} = \phi\sigma^s_{ij} + (1-\phi)\sigma^f_{ij}, \tag{8}$$

and by using such a mixture model for stress, we essentially satisfy the dynamic interaction condition (4) at the fluid–solid interface.

In the fluid domain, we consider Newtonian fluid, and therefore, the fluid stress is prescribed as

$$\sigma^f_{ij} = 2\mu^f D_{ij}, \tag{9}$$

where μ^f is the fluid dynamic viscosity and D_{ij} is a component of the strain-rate tensor $\boldsymbol{D}$,

$$D_{ij} = \frac{1}{2}\left(\frac{\partial u_i}{\partial x_j} + \frac{\partial u_j}{\partial x_i}\right). \tag{10}$$

In the solid domain, we consider viscous hyperelastic material, and therefore, the solid stress is prescribed as

$$\sigma^s_{ij} = 2\mu^s D_{ij} + \sigma^{hy}_{ij}, \tag{11}$$

where $2\mu^s D_{ij}$ is the viscous contribution and σ^{hy}_{ij} is the hyperelastic stress contribution. We consider the mechanical behavior of linear and nonlinear hyperelastic materials that satisfy the incompressible Mooney–Rivlin law [72, 73] and are often used to model biological and soft rubber-like materials. Specifically, we consider neo-Hookean and Saint Venant-Kirchhoff materials that are subsets of linear and nonlinear Mooney–Rivlin materials, respectively [10, 49].

For the neo-Hookean material, the hyperelastic stress is prescribed as [10, 49]

$$\sigma^{hy}_{ij} = G^s(B_{ij} - \delta_{ij}), \tag{12}$$

where G^s is the modulus of transverse elasticity, B_{ij} is a component of the left Cauchy–Green deformation tensor $\boldsymbol{B}$, and δ_{ij} is the Kronecker delta function.

For the Saint Venant-Kirchhoff material, the hyperelastic stress is modeled as [10, 49]

$$\sigma^{hy}_{ij} = G^s(B_{ik}B_{kj} - B_{ij}). \tag{13}$$

As the upper convected time derivative of $\boldsymbol{B}$ is identically zero [49, 74], we can update $\boldsymbol{B}$ as

$$\frac{\partial B_{ij}}{\partial t} + u_k\frac{\partial B_{ij}}{\partial x_k} = B_{ik}\frac{\partial u_j}{\partial x_k} + B_{kj}\frac{\partial u_i}{\partial x_k}. \tag{14}$$

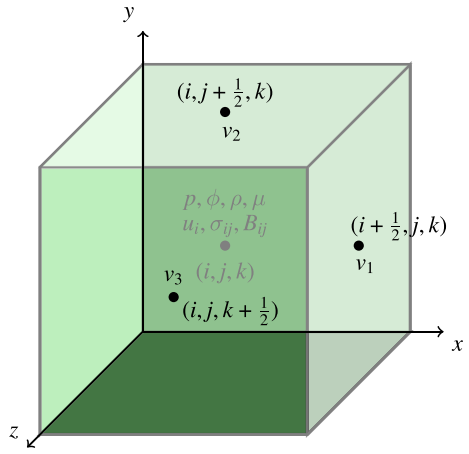

FIGURE 2 | Location of variables for a three-dimensional unit computational cell. ● cell center; ● face center. [Colour figure can be viewed at wileyonlinelibrary.com]

2.2 | Numerical Details

We use an Eulerian VOF model similar to Sugiyama et al. [49] to simulate the interaction of incompressible flow and incompressible viscous hyperelastic structures on a fixed Cartesian grid. The fluid–solid interface is captured using the geometric VOF procedure that ensures a sharp interface. We first reconstruct the interface in each computational cell using PLIC method [64–67] and then perform a directionally split advection procedure to exchange volume fraction across cell boundaries using LE method [58, 61, 68]. The transport equation of $\boldsymbol{B}$ tensor (14) is solved using the finite difference method (FDM) utilizing the fifth-order weighted essentially non-oscillatory (WENO-Z) [50, 69] finite difference reconstruction procedure, as the fifth-order WENO scheme [50] was shown to work well by Sugiyama et al. [49] However, the unified momentum conservation equations with incompressibility constraints (6) are solved using a FVM [70] that was developed for incompressible flows with a focus on discrete kinetic energy conservation in the inviscid limit and is robust at high Reynolds numbers. The FSI solver is built on the framework of our in-house FVM solver that has been extensively used in the past to investigate a variety of problems such as flow over superhydrophobic surfaces [75, 76], random roughness surfaces [77], and roughness elements [78, 79]. It has also been used to analyze sources of turbulent wall-pressure fluctuations [80] and provide turbulent wall-pressure forcing to excite elastic plate vibrations [56, 57].

The problem is discretized such that the velocity (u_i), stress (σ_{ij}), left Cauchy–Green deformation tensor ($\boldsymbol{B}$), pressure (p), solid volume fraction (ϕ), density (ρ), and viscosity (μ) are defined at the cell center; the face-normal velocities (v_n) are defined at the center of the cell faces. Figure 2 shows the location of variables for a three-dimensional unit computational cell.

2.2.1 | Time Advancement and Spatial Discretizations

To describe the initial shape of the solid structure, we prescribe the corresponding ϕ distribution on the fixed Cartesian grid. In

addition, we set $\boldsymbol{B} = \boldsymbol{I}$ in the whole domain, corresponding to the initial unstressed state of the solid system, where $\boldsymbol{I}$ is the unit tensor. Such a simple definition facilitates handling multicomponent solid systems and complex geometries.

We update the variables at $\{n+1\}$th timestep from the previous timesteps ($\{n\}$, $\{n-1\}$) in four steps:

Step 1: Update ϕ using geometric VOF method. The details are discussed in Section 2.2.2.

Step 2: Update $\boldsymbol{B}$ tensor. We use the second-order Adams–Bashforth scheme to update $\boldsymbol{B}$,

$$B_{ij}^{n+1} = B_{ij}^{n} + \Delta t \times \left[\frac{3}{2}\left(B_{ik}\frac{\partial u_j}{\partial x_k} + B_{kj}\frac{\partial u_i}{\partial x_k}\right)^{n} - \frac{1}{2}\left(B_{ik}\frac{\partial u_j}{\partial x_k} + B_{kj}\frac{\partial u_i}{\partial x_k}\right)^{n-1}\right] - \Delta t\left[\frac{3}{2}\left(u_k\frac{\partial B_{ij}}{\partial x_k}\right)^{n} - \frac{1}{2}\left(u_k\frac{\partial B_{ij}}{\partial x_k}\right)^{n-1}\right], \tag{15}$$

where the time step Δt is set such that the CFL numbers based on advection speed and shear wave speed are less than 0.5.

Step 3: Fractional step—predict velocity while omitting the pressure contribution. We use an implicit Crank–Nicolson time advancement scheme to predict the cell-centered velocity,

$$\frac{u_i^* - u_i^n}{\Delta t} = \frac{1}{2}\left[\left(\frac{1}{\rho}\frac{\partial \sigma_{ij}}{\partial x_j} - \frac{\partial u_i u_j}{\partial x_j}\right)^{n} + \left(\frac{1}{\rho}\frac{\partial \sigma_{ij}}{\partial x_j} - \frac{\partial u_i u_j}{\partial x_j}\right)^{n+1}\right], \tag{16}$$

where we linearize the nonlinear convection terms and set u_i^{n+1} as u_i^*. We perform symmetric interpolation ($O(\Delta_x^2)$) to obtain the face-normal velocities from the cell-centered velocities,

$$v_n = \left(\frac{u_{cv1} + u_{cv2}}{2}\right), \tag{17}$$

where u_{cv1} and u_{cv2} are the cell-centered velocity components of control volumes (CVs) $cv1$ and $cv2$ that share the considered face. Also, u_{cv1} and u_{cv2} are aligned in the face-normal direction.

Step 4: Fractional step—correct velocity using the pressure distribution yielded from the incompressibility constraint. We project the corrector step,

$$\frac{u_i^{n+1} - u_i^*}{\Delta t} = -\frac{1}{\rho}\frac{\partial p^{n+1}}{\partial x_i}, \tag{18}$$

on the face-normal,

$$\frac{v_n^{n+1} - v_n^*}{\Delta t} = -\frac{1}{\rho}\frac{\partial p^{n+1}}{\partial n}, \tag{19}$$

and solve the Poisson equation derived using the incompressibility constraint to obtain the pressure distribution,

$$\sum_{k=1}^{N_{faces}} \frac{\Delta t}{\rho}\frac{\partial p^{n+1}}{\partial n} A_k = \sum_{k=1}^{N_{faces}} v_n^* A_k, \tag{20}$$

where $k = 1, 2, \ldots, N_{faces}$ correspond to the faces of a CV and A_k is the face area. The Poisson equation is solved using the multigrid preconditioned conjugate gradient (CG) method utilizing the Trilinos libraries (Sandia National Labs). Finally, we correct the predicted velocity using the pressure gradient,

$$\frac{u_i^{n+1} - u_i^*}{\Delta t} = -\frac{1}{\rho}\frac{\partial p^{n+1}}{\partial x_i}. \tag{21}$$

In the above time advancement equations, we compute the derivatives (except for the advection terms involved in Equation (15)) by computing the derivative at faces and using symmetric interpolation as required. The derivative terms at the face center are defined as

$$\frac{\partial(\cdot)}{\partial n} = \frac{(\cdot)_{cv2} - (\cdot)_{cv1}}{\Delta_f}, \tag{22}$$

where the face-normal n points from $cv1$ to $cv2$ and $\Delta_f = (x_{i,cv2} - x_{i,cv1})$. For the advection term involved in Equation (15), we use the fifth-order WENO-Z finite difference reconstruction procedure (discussed in Section 2.2.3).

2.2.2 | Geometric VOF (VOF/PLIC) Interface-Capturing Method

Given a material boundary consisting of a fluid and a solid (or any two phases) sharing an interface at a particular location $\mathbf{x}$, the Heaviside function $H(\mathbf{x}, t)$ is defined as

$$H(\mathbf{x}, t) = \begin{cases} 0, & \text{if } \mathbf{x} \in \Omega^f, \\ 1, & \text{if } \mathbf{x} \in \Omega^s, \end{cases} \tag{23}$$

where Ω_f and Ω_s refer to the fluid and solid subdomains, respectively. As the interface moves and deforms, the shape of each phase changes, however both materials are considered insoluble so that the material derivative of H remains zero such that:

$$\frac{DH}{Dt} = \frac{\partial H}{\partial t} + \mathbf{u}.\nabla H = 0, \tag{24}$$

where $\mathbf{u}$ represents the monolithic velocity of the one-fluid formulation described in Section 2.1. Using the vector identity $\nabla \cdot (\mathbf{u}H) = \mathbf{u} \cdot \nabla H + H(\nabla \cdot \mathbf{u})$, the advection equation becomes:

$$\frac{\partial H}{\partial t} + \nabla \cdot (\mathbf{u}H) = H(\nabla \cdot \mathbf{u}). \tag{25}$$

The volume fraction ϕ, often referred to as the color function, is used to define the numerical approximation of the Heaviside function as the spatial average of H in each computational cell such that,

$$\phi_{ijk} = \frac{1}{V_c}\int_{\Omega_c} H(\mathbf{x}, t)\mathrm{d}V, \tag{26}$$

where Ω_c represents the volume integral over the cell volume, $V_c = \int_{\Omega_c} \mathrm{d}V$ is the cell volume, and the subscripts i, j, and k denote the index locations of the control volume on the Cartesian grid in the x, y, and z directions, respectively. As mentioned earlier, by definition, $\phi = 0$ in the fluid domain, $\phi = 1$ in the solid

domain, and $\phi \in (0,1)$ at the fluid–solid interface. After integrating Equation (25) over a computational cell and substituting Equation (26) in the integral, the resulting equation becomes:

$$V_c \frac{\partial \phi_{ijk}(t)}{\partial t} + \oint_{\partial\Omega_c} (\mathbf{u}\cdot\mathbf{n}) H(\mathbf{x},t) dA = \int_{\Omega_c} H(\mathbf{x},t)(\nabla\cdot\mathbf{u}) dV, \tag{27}$$

where $\partial\Omega_c$ is the cell boundary line and $\mathbf{n}$ is the outgoing unit normal. In the case of incompressibility $\nabla\cdot\mathbf{u}$ is equal to zero, nonetheless, the appearance of the right-hand side in Equation (27) is related to the implementation details of the directionally split advection, where the sum of the divergence contribution from each Cartesian direction should add up to zero and is not zero individually. We refer the reader to Tryggvason et al. [43] for further details about the discretization process of the advection equation.

In the geometric VOF method, the interface is approximated geometrically in a computational cell. The methodology can be summarized in two fundamental steps: the reconstruction step and the advection step.

Reconstruction step:

In the reconstruction step, we find the interface location in each computational cell using the PLIC technique [64–67]. It involves two steps: (i) estimating the normal direction of the interface and (ii) geometrically shifting the interface location along the normal direction to attain the required volume under the interface.

We estimate the normal ($\mathbf{m}$) of the local interface as $\mathbf{m} = m_i \mathbf{e}_i = -\nabla_{\delta_{x_i}} \phi$ using Young's FDM [66, 67], where the finite difference approximation of the normals at the cell corners are used to compute the normals at the cell centers. For 2D problems with uniform cells, the normal components at the cell corner are estimated as,

$$m_{x:i+\frac{1}{2},j+\frac{1}{2}} = -\frac{1}{2\Delta_x}\left(\phi_{i+1,j} - \phi_{i,j} + \phi_{i+1,j+1} - \phi_{i,j+1}\right), \tag{28}$$

$$m_{y:i+\frac{1}{2},j+\frac{1}{2}} = -\frac{1}{2\Delta_y}\left(\phi_{i,j+1} - \phi_{i,j} + \phi_{i+1,j+1} - \phi_{i+1,j}\right), \tag{29}$$

where Δ_x and Δ_y are the grid spacing in x and y directions, respectively. Then, we compute the components at the cell center as,

$$m_{x/y:i,j} = \frac{1}{4}\left(m_{x/y:i-\frac{1}{2},j-\frac{1}{2}} + m_{x/y:i+\frac{1}{2},j-\frac{1}{2}} + m_{x/y:i+\frac{1}{2},j+\frac{1}{2}} + m_{x/y:i-\frac{1}{2},j+\frac{1}{2}}\right). \tag{30}$$

Similarly, we estimate normals for 3D problems and represent the interface as,

$$m_{x:i,j,k} x + m_{y:i,j,k} y + m_{z:i,j,k} z = \beta_{i,j,k}, \tag{31}$$

and we use the analytical relations [81] to adjust $\beta_{i,j,k}$ such that the local solid volume under the interface is equal to $\phi_{i,j,k} V_c$, where V_c is the cell volume.

Advection step:

In the advection step, we use the directionally split advection procedure where LE [58, 61, 68] geometrical linear-mapping method is used to exchange the reference volume fraction across the cell boundaries. Each timestep involves three directionally split advection substeps for 3D problems, where $\phi^{(n,l+1)}$ is estimated using $\phi^{(n,l)}$, where $l = 1, 2, 3$ corresponds to the directional sweeps, $\phi^{(n,1)} = \phi^n$, and $\phi^{(n,4)} = \phi^{n+1}$. Before each advection substep, we reconstruct the interface to be consistent with $\phi^{(n,l)}$. As a result, each timestep involves three reconstruction steps and three advection steps. To avoid preferential direction, the directional sweeps are rotated cyclically.

To advect the reconstructed interface in x_d direction, we use a linearized velocity field to move the endpoints of the interface segment in each cell. We rescale space and time using the local grid spacing (Δx_d) and time step (Δt). It yields the following non-dimensional variables: $x_d^* = x_d/\Delta x_d$, $t^* = t/\Delta t$, and $u_d^* = u_d \Delta t/\Delta x_d$, where the non-dimensional velocity is the local CFL number. Such rescaling enables the IC algorithm to efficiently handle cuboidal cells, as all the cells are mapped to a unit cube. For brevity, superscript "*" is dropped in the following discussion.

The general LE steps are summarized below.

Step 1: Translate the reconstructed segments using the equation $x_d(t^{n+1}) = (1 + u_{d+} - u_{d-})x_d + u_{d-}$, where the left face is considered as the origin for x_d, u_{d-} is the left face velocity, and u_{d+} is the right face velocity. This expression is obtained by integrating the equation of motion using an explicit first-order scheme ($dx_d/dt = u_d(x_d)$) and linearly interpolating velocity ($u_d(\mathbf{x}) = u_{d-}(1 - x_d) + u_{d+}x_d$).

Step 2: Update the volume fraction by accounting for the contributions from the neighboring cells, that is, $\phi_{i,j,k}^{(n,l+1)} = \Phi_1^d + \Phi_2^d + \Phi_3^d$, where Φ_2^d corresponds to the contribution from the cell itself, and Φ_1^d and Φ_3^d corresponds to the contribution from the left and right cells, respectively. Figure 3 shows a simple representation of these volume contributions for a 2D cell.

Step 3: Scale all the measures of space using the "compression" factor $(1 + u_{d+} - u_{d-})$ in the cell region, translate the cells by u_{d-}, and the final update can be expressed as $\phi_{i,j,k}^{(n,l+1)} = \phi_{i,j,k}^{(n,l)}(1 + u_{d+} - u_{d-}) - F_{d+} + F_{d-}$, where F_{d-} corresponds to the flux of $u_d H$ at the left face and F_{d+} corresponds to the flux at the right face.

To avoid the unwanted effects of the arithmetic floating-point round-off error, we perform the clipping procedure after each directional sweep. We set $\phi_{i,j,k} = 0$ if $\phi_{i,j,k} < \epsilon_c$ and $\phi_{i,j,k} = 1$ if $\phi_{i,j,k} > 1 - \epsilon_c$, where the clipping tolerance ϵ_c is set to 10^{-8} for all the problems. For more details, we refer the reader to Alamé [68]. To prevent the exponential growth of $\boldsymbol{B}$ near the interface due to the shearing motion in the fluid domain, we set $\boldsymbol{B} = \boldsymbol{I}$ for $\phi_{i,j,k} < \epsilon_c$.

2.2.3 | Fifth-Order WENO-Z Finite Difference Reconstruction

The fifth-order WENO-Z finite difference reconstruction procedure [50, 69] is used to treat the advection terms involved in

the transport equation of $\boldsymbol{B}$ tensor (15), as the fifth-order WENO scheme [50] was shown to perform well by Sugiyama et al. [49]. We discuss the reconstruction procedure to treat the advection term involved in the one-dimensional transport equation of a scalar f,

$$\frac{\partial f}{\partial t} + u\frac{\partial f}{\partial x} = 0, \tag{32}$$

and a similar procedure is used to treat the advection terms involved in the 3D transport equation of the $\boldsymbol{B}$ tensor.

We consider the compact upwind/downwind form [82] of the above transport equation,

$$\frac{\partial f_i}{\partial t} + u_i^p\left(\frac{\tilde{f}^+_{i+\frac{1}{2}} - \tilde{f}^+_{i-\frac{1}{2}}}{\Delta_x}\right) + u_i^m\left(\frac{\tilde{f}^-_{i+\frac{1}{2}} - \tilde{f}^-_{i-\frac{1}{2}}}{\Delta_x}\right) = 0, \tag{33}$$

where f_i is the cell-centered value of f on a uniform grid with Δ_x spacing, $u_i^p = \max(u_i, 0)$, $u_i^m = \min(u_i, 0)$, $\tilde{f}$ is a high-order reconstruction of f, and the superscripts $+$ and $-$ reflect correspondence to positive (u_i^p) and negative (u_i^m) cell-center velocities, respectively.

The reconstruction procedure for $\tilde{f}^+_{i+\frac{1}{2}}$ (referred to as $g_{i+\frac{1}{2}}$) is discussed, and the procedure for $\tilde{f}^-_{i+\frac{1}{2}}$ is similar with symmetry about $x_{i+\frac{1}{2}}$. We use a 5-point stencil ($S^5 = \{x_{i-2}, x_{i-1}, x_i, x_{i+1}, x_{i+2}\}$) to compute $g_{i+\frac{1}{2}}$ and it comprises of three 3-point stencils ($S^0 = \{x_{i-2}, x_{i-1}, x_i\}, S^1 = \{x_{i-1}, x_i, x_{i+1}\}, S^2 = \{x_i, x_{i+1}, x_{i+2}\}$), as shown in Figure 4.

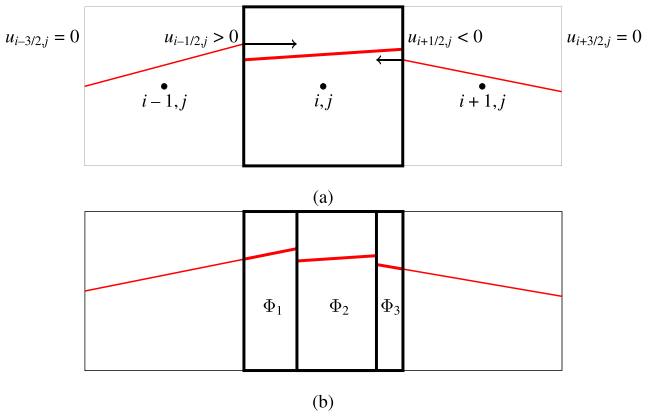

FIGURE 3 | (a) Reconstructed interface with horizontal velocities and (b) volume formation (Φ_i) for the central cell by the Lagrangian advection in x direction. [Colour figure can be viewed at wileyonlinelibrary.com]

We compute $g_{i+\frac{1}{2}}$ as

$$g_{i+\frac{1}{2}} = \sum_{j=0}^{2} \omega_j g^j_{i+\frac{1}{2}}, \tag{34}$$

where $g_{i+\frac{1}{2}}$ is computed as a convex combination of interpolated values $g^j_{i+\frac{1}{2}}$ on 3-point stencils,

$$g^j_{i+\frac{1}{2}} = \sum_{k=0}^{2} \alpha_{jk} f_{i+j+k-2}, \tag{35}$$

the weights ω_j correspond to 3-point stencils S^j, and the coefficients α_{jk} for all 3-point stencils are given by Jiang and Shu [50] as shown in Table 1.

The weights ω_j are defined using smoothness indicators IS_j that estimates the smoothness of f over each stencil S_j. We consider the non-oscillatory weights suggested by Borges et al. [69], where Borges et al. [69] developed an improved version of the classical WENO-JS [50] scheme to decrease dissipation and increase resolution. The non-oscillatory weights and smoothness indicators are given below.

Borges et al. [69] used the 5-point stencil S^5 to define the smoothness indicators,

$$IS^Z_j = \left(\frac{IS^{JS}_j + \epsilon}{IS^{JS}_j + IS^Z_5 + \epsilon}\right), \quad j = 0, 1, 2, \tag{36}$$

where the smoothness indicators IS^{JS}_j are defined by Jiang and Shu [50] as

$$IS^{JS}_0 = \frac{13}{12}(f_{i-2} - 2f_{i-1} + f_i)^2 + \frac{1}{4}(f_{i-2} - 4f_{i-1} + 3f_i)^2, \tag{37}$$

$$IS^{JS}_1 = \frac{13}{12}(f_{i-1} - 2f_i + f_{i+1})^2 + \frac{1}{4}(f_{i-1} - f_{i+1})^2, \tag{38}$$

$$IS^{JS}_2 = \frac{13}{12}(f_i - 2f_{i+1} + f_{i+2})^2 + \frac{1}{4}(3f_i - 4f_{i+1} + f_{i+2})^2, \tag{39}$$

the smoothness indicator IS^Z_5 is defined by Borges et al. [69] as

$$IS^Z_5 = \left|IS^{JS}_0 - IS^{JS}_2\right|, \tag{40}$$

and the corresponding weights ω^Z_j are defined as

$$\omega^Z_j = \frac{\beta^Z_j}{\beta^Z_0 + \beta^Z_1 + \beta^Z_2}, \quad \beta^Z_j = \frac{\gamma^{JS}_j}{IS^Z_j} = \gamma^{JS}_j\left(1 + \frac{IS^Z_5}{IS^{JS}_j + \epsilon}\right), \tag{41}$$

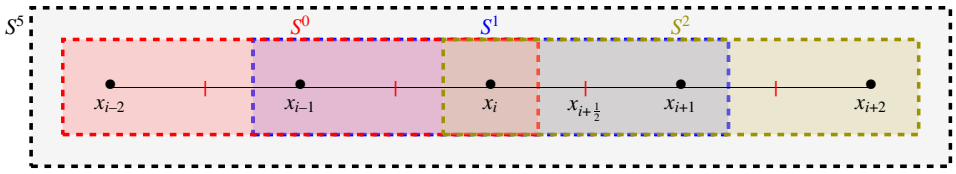

FIGURE 4 | Stencils involved in the fifth-order WENO reconstruction of $g_{i+\frac{1}{2}}$. [Colour figure can be viewed at wileyonlinelibrary.com]

where $\gamma_0^{JS} = 1/10$, $\gamma_1^{JS} = 6/10$, $\gamma_2^{JS} = 3/10$ are the coefficients proposed by Jiang and Shu [50], and $\epsilon = 10^{-40}$ is a small constant used to avoid division by zero.

3 | Numerical Experiments

To assess the performance of the FSI solver, we consider multiple benchmark problems: rigid body motion of a slotted disk [83], compliant wall in a lid-driven cavity [42, 84, 85], circular disk in a lid-driven cavity [42, 49], disk in a shear flow [10], and sphere in a lid-driven cavity [86, 87]. Furthermore, we use the framework to perform direct numerical simulation (DNS) of turbulent channel flow with a deformable compliant bottom wall and a rigid top wall.

3.1 | Rigid Body Motion of a Slotted Disk

To validate the VOF/PLIC method, we simulate the rigid body motion of a slotted disk [83] in a prescribed velocity field. Initially, the slotted disk is centered at $(0.5, 0.75)$ with a radius of $r = 0.15$ and a slot that is $l = 0.2$ deep and $w = 0.06$ wide. The computational domain is a unit square ($L_x \times L_y = 1 \times 1$). The disk undergoes rigid body motion in the prescribed velocity field,

$$u(y) = 2\pi(y - y_c), \quad v(x) = -2\pi(x - x_c), \tag{42}$$

where $(x_c, y_c) = (0.5, 0.5)$ is the center of rotation. At $t = 1$, the disk completes one cycle of rotation in the velocity field, as shown in Figure 5.

TABLE 1 | Coefficients α_{jk} for fifth-order WENO reconstruction [50].

j	$k = 0$	$k = 1$	$k = 2$
0	1/3	−7/6	11/6
1	−1/6	5/6	1/3
2	1/3	5/6	−1/6

The performance of the VOF/PLIC method improves with grid resolution. Figure 6 compares the disk shape ($\phi = 0.5$) after one cycle ($t = 1$) for different grid sizes ($N_x \times N_y$, where N_x and N_y are the number of computational cells in x and y directions, respectively) with the initial shape ($t = 0$) on 512×512 grid. Increasing the grid size decreases the difference between the initial and final shape of the slotted disk, especially near the corners.

We compute L_1 shape error (E_1) to quantify the accuracy of the VOF/PLIC method,

$$E_1(N = N_x) = \frac{1}{N_x N_y} \sum_{i=1}^{N_x} \sum_{j=1}^{N_y} \left| \phi_{i,j}(t = 1) - \phi_{i,j}(t = 0) \right|. \tag{43}$$

For all the grids considered, $N_x = N_y = N$. Figure 7 shows the variation of $L_1(N)$ with N, where the error roughly decreases as N^{-1} for higher grid resolutions.

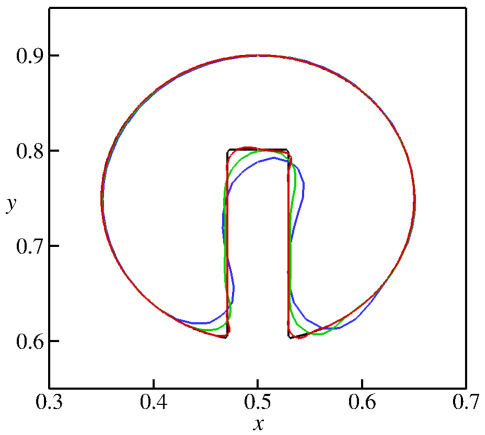

FIGURE 6 | Rigid slotted disk shape. — 512×512 ($t = 0$); — 64×64 ($t = 1$); — 128×128 ($t = 1$); — 512×512 ($t = 1$). [Colour figure can be viewed at wileyonlinelibrary.com]

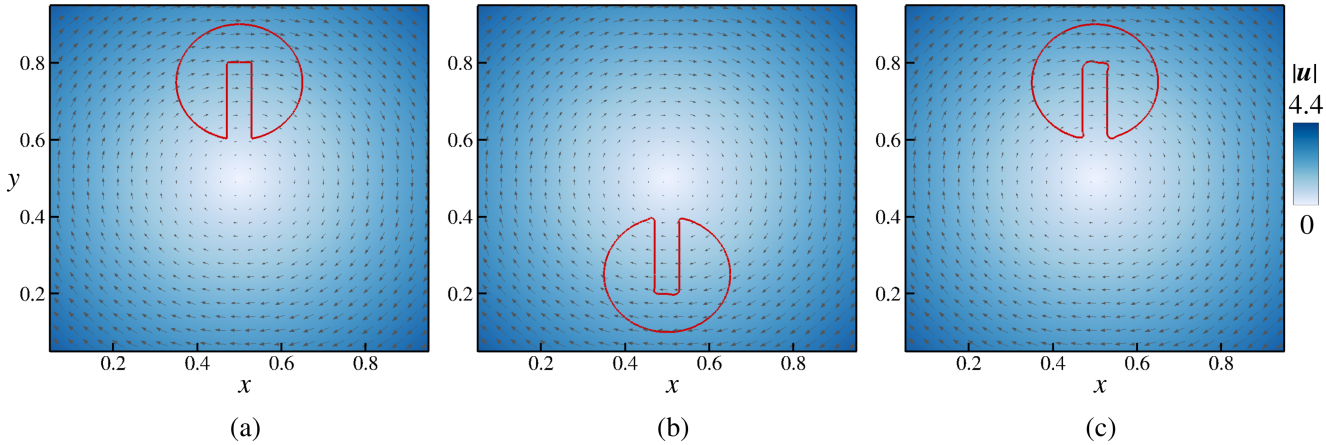

FIGURE 5 | Rigid slotted disk in a prescribed velocity field at (a) $t = 0$, (b) $t = 0.5$, and (c) $t = 1$. The red curve shows the slotted disk shape ($\phi = 0.5$), the filled contours show velocity magnitude, and the arrows represent velocity vectors. The unit square domain is discretized using $N_x \times N_y = 512 \times 512$ cells. [Colour figure can be viewed at wileyonlinelibrary.com]

3.2 | Compliant Wall in a Lid-Driven Cavity

We simulate the motion of an incompressible neo-Hookean compliant wall at the bottom of a lid-driven cavity [42, 84, 85]. The cavity size is $L_x \times L_y = 2 \times 2$ and the grid size is $N_x \times N_y = 512 \times 512$. Initially, the system is at rest, and the unstressed compliant wall has a flat interface. The thickness of the compliant wall is $h^s = 0.5$. The solid material properties are $G^s = 0.2$, $\mu^s = 0.2$, and $\rho^s = 1$. The fluid properties are $\mu^f = 0.2$ and $\rho^f = 1$. The cavity is driven by the top wall that moves with a non-uniform velocity distribution,

$$V_w(x) = 0.5\begin{cases}\sin^2(\pi x/0.6), & \text{if } x \in [0, 0.3],\\ 1, & \text{if } x \in (0.3, 1.7),\\ \sin^2(\pi(x-2)/0.6), & \text{if } x \in [1.7, 2],\end{cases} \tag{44}$$

and the other walls are stationary. Similar to Zhao et al. [42], the momentum convection is ignored.

The VOF/PLIC method ensures that the fluid–solid interface remains sharp throughout the time history, and our compliant wall deformation obtained on an Eulerian grid is in excellent agreement with that of Zhao et al. [42] obtained using a Lagrangian solid mesh. Figure 8 shows ϕ distribution inside the lid-driven cavity at $t = 0$ and steady state ($t = 8$). The fluid–solid interface at steady state is as sharp as at $t = 0$. At steady state, the interface shape agrees well with the result of Zhao et al. [42], and the streamlines are centered along the x-direction, similar to past works [42, 54, 84].

Figure 9 shows the variation of pressure and velocity with y in the cavity at $x = 0.5$ (Figure 9a) and $x = 1.5$ (Figure 9b). As the VOF/PLIC method maintains a sharp fluid–solid interface, the pressure jump near the interface is captured well.

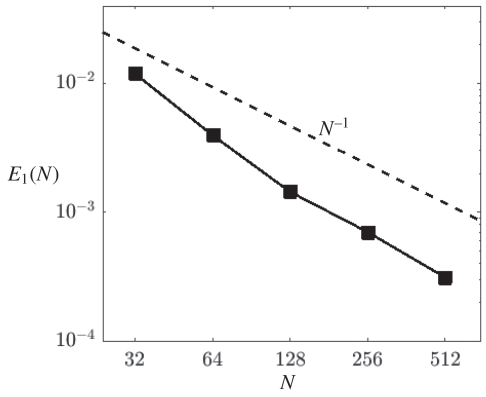

FIGURE 7 | L_1 shape error ($E_1(N)$) for rigid slotted disk.

3.3 | Disk in a Lid-Driven Cavity

We simulate the motion of an incompressible neo-Hookean solid disk in a lid-driven cavity [42, 49]. The cavity dimensions are $L_x \times L_y = 1 \times 1$ and the grid size is $N_x \times N_y = 128 \times 128$. The system is at rest initially. The top wall starts moving with a constant velocity $V_w = 1$ in x direction, and the remaining boundaries of the cavity stay stationary. The unstressed solid has a circular shape centered at $(x_c, y_c) = (0.6, 0.5)$ with a radius of $r = 0.2$. The density and viscosity of the fluid and solid domains are the same, that is, $\rho^s = \rho^f = 1$ and $\mu^s = \mu^f = 0.01$. We consider two disks: soft disk with $G^s = 0.1$ and stiff disk with $G^s = 10$.

At all time instants, the deformed solid shapes are in excellent agreement with the references. Figure 10 shows the soft disk shape and cavity flow at different time instants obtained using the VOF/PLIC-based FSI framework (referred to as VOF/PLIC in figures for brevity), along with results of Sugiyama et al. [49] obtained on 1024×1024 Eulerian grid. The shape and location of the soft solid agree well with the reference. Figure 11 shows the stiff disk shape and cavity flow at different time instants, along with results of Zhao et al. [42] obtained using a Lagrangian solid mesh. For all instances, the shape and location of the stiff solid also agree well with the reference.

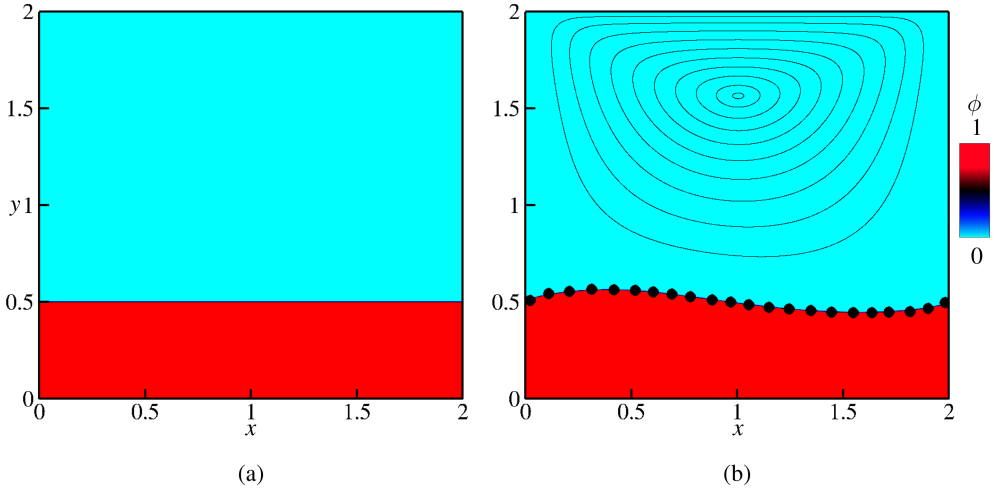

FIGURE 8 | Compliant wall in a lid-driven cavity at (a) $t = 0$ and (b) steady state ($t = 8$). Filled contours show ϕ. In (b), thin black lines represent streamlines, and black circles (●) indicate deformed compliant surface as reported by Zhao et al. [42]. [Colour figure can be viewed at wileyonlinelibrary.com]

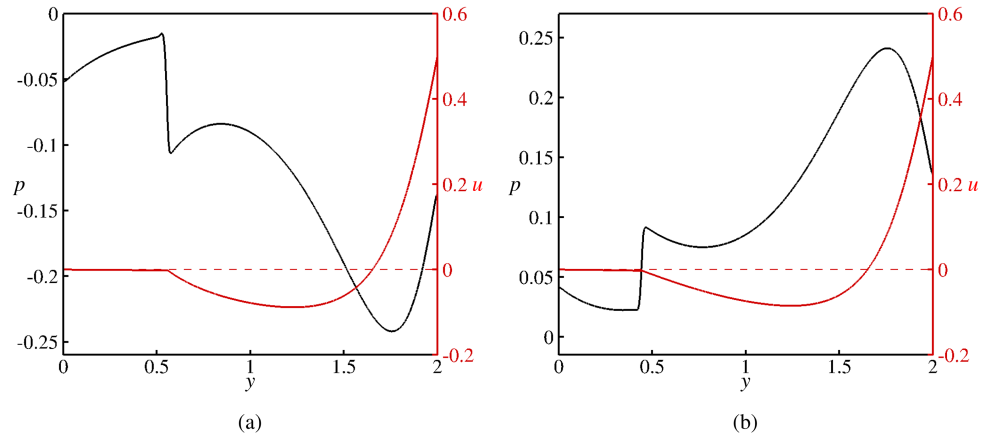

FIGURE 9 | Pressure and velocity distribution at (a) $x = 0.5$ and (b) $x = 1.5$ inside the lid-driven cavity with a compliant wall. — p; — u; - - - $u = 0$. [Colour figure can be viewed at wileyonlinelibrary.com]

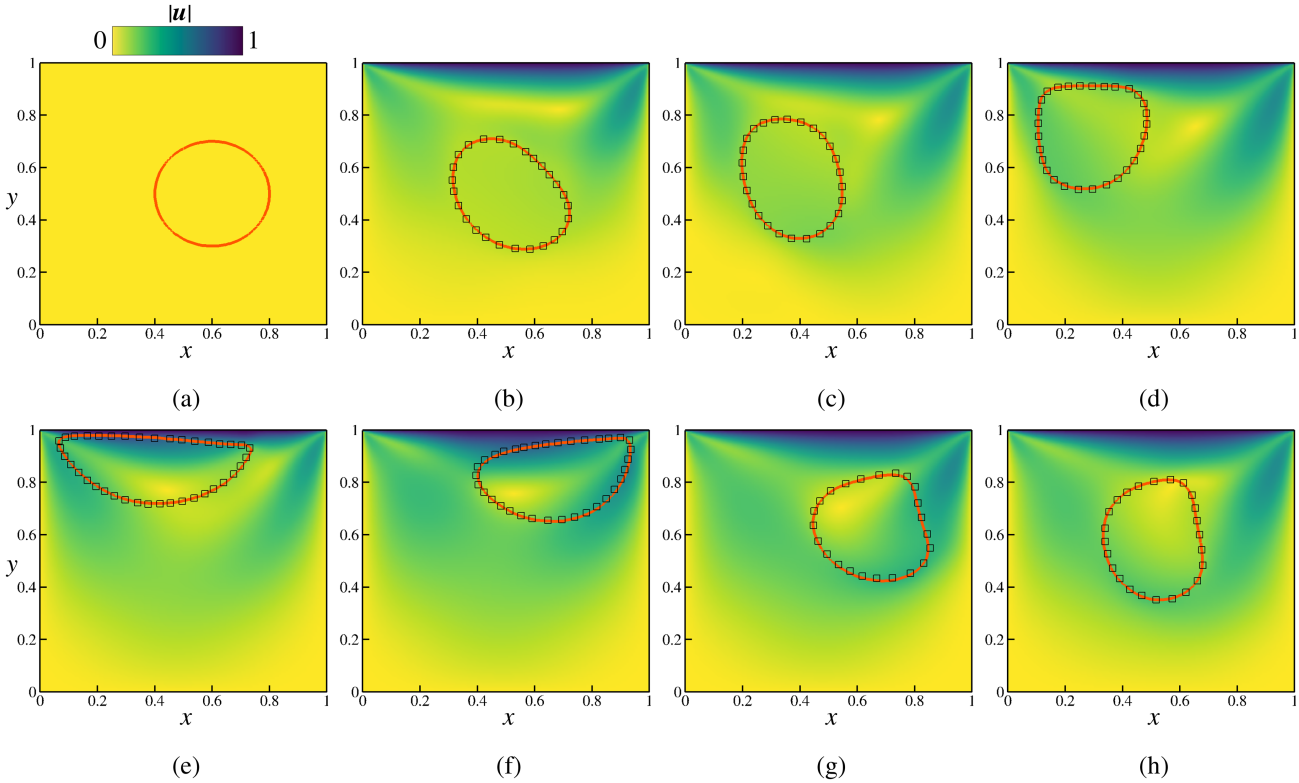

FIGURE 10 | Soft solid ($G^s = 0.1$) in a lid-driven cavity at different time instants. (a-h) $t = 0, 1.17, 2.34, 3.52, 4.69, 5.86, 7.03, 8.20$; — VOF/PLIC (solid shape on 128×128 grid); □ Sugiyama et al. [49] (solid shape on 1024×1024 grid). The filled contours show flow speed. [Colour figure can be viewed at wileyonlinelibrary.com]

Once the lid starts moving, the solid moves toward the top lid due to the flow circulation, where the soft solid undergoes significant deformation, while the stiff solid behaves like a nearly rigid body. However, due to the lubrication effect [88] between the solid and the wall, the solid does not touch the top lid.

The VOF/PLIC-based FSI framework does not generate unphysical solid fragments even when the solid undergoes significant deformation or has a high pinching tendency. The soft disk experiences high stretching near the top lid ($t = 4.69$ in Figure 10) before it slides along the lid. As a result, one of the corners (right) has the highest tendency to undergo pinching which could lead to non-physical solid fragments ejecting from the main body in the following time. The time instants $t = 4.69, 5.86, 7.03$, and 8.20 in Figure 10 verify that no such mass fragments are generated.

To further verify the results and show grid convergence, we compute the solid centroid trajectory [49],

$$\boldsymbol{x}_c(t) = \frac{\sum_{i=1}^{N_x}\sum_{j=1}^{N_y}\boldsymbol{x}_{i,j}\phi_{i,j}(t)\Delta_x\Delta_y}{\sum_{i=1}^{N_x}\sum_{j=1}^{N_y}\phi_{i,j}(t)\Delta_x\Delta_y}, \tag{45}$$

for the soft solid.

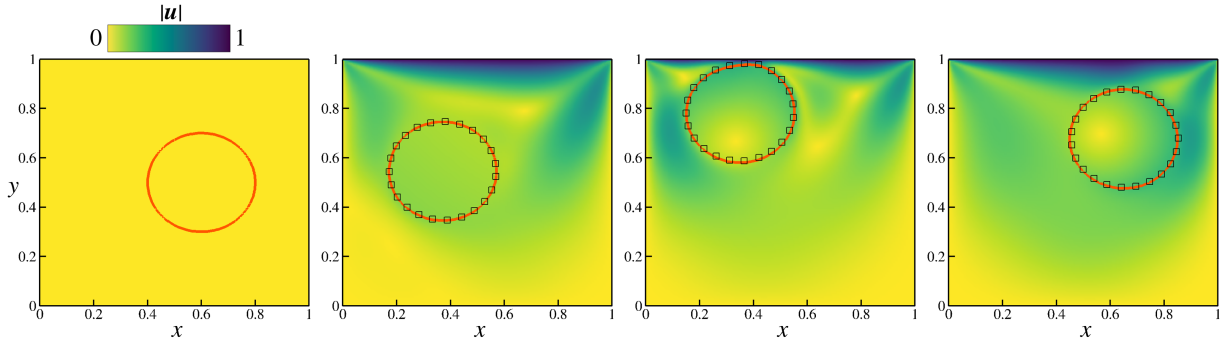

FIGURE 11 | Stiff solid ($G^s = 10$) in a lid-driven cavity at different time instants. (a-d) $t = 0, 2.34, 4.69, 7.03$; — VOF/PLIC (solid shape); □ Zhao et al. [42] (solid shape). The filled contours show flow speed. [Colour figure can be viewed at wileyonlinelibrary.com]

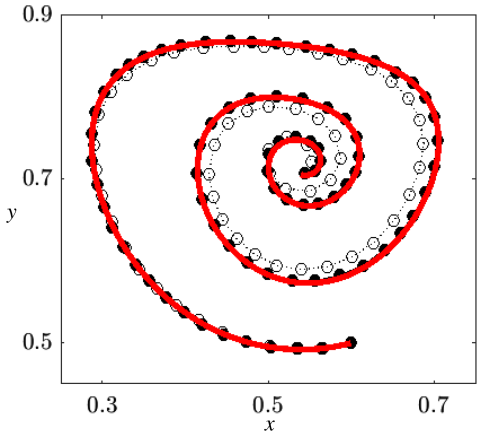

FIGURE 12 | Soft solid centroid trajectory for $t \in [0, 20]$. — VOF/PLIC (128×128); ● Sugiyama et al. [49] (1024×1024); ○ Sugiyama et al. [49] (128×128). [Colour figure can be viewed at wileyonlinelibrary.com]

The accuracy of our VOF/PLIC-based FSI approach on coarse grids is comparable to the accuracy of a diffusive IC method-based FSI approach on much finer grids. Figure 12 shows the soft solid centroid trajectory for $t \in [0, 20]$. Our centroid trajectory obtained on 128×128 Eulerian grid matches well with that of Sugiyama et al. [49] obtained on 1024×1024 Eulerian grid using a fifth-order WENO scheme to advect the interface. Furthermore, as discussed above, at all time instances (Figure 10), the deformed soft solid shapes on 128×128 grid are in excellent agreement with those of Sugiyama et al. [49] on 1024×1024 grid. It reflects the advantage of using the VOF/PLIC method to capture the fluid–solid interface that maintains a sharp interface, whereas WENO diffuses it.

To analyze grid convergence, Figure 13a shows the soft solid centroid trajectory for various grid sizes (64×64, 128×128, 256×256, 512×512, 1024×1024). For grid sizes greater than 128×128, there are negligible differences in the centroid trajectory, indicating grid convergence at 128×128 grid size.

To evaluate the order of convergence, we compute L_2 error defined as

$$E_2(N = N_x) = \left[\frac{1}{T}\int_0^T |\boldsymbol{x}_c(t, N_x) - \boldsymbol{x}_c(t, N_x = 1024)|^2 \mathrm{d}t\right]^{0.5}. \quad (46)$$

Figure 13b shows E_2 monotonically decreases with grid size and the order of convergence is approximately first-order (N^{-1}) for smaller grid sizes.

Furthermore, to verify the grid convergence of the flow variables, we consider the velocity distribution inside the lid-driven cavity with a soft disk. Figure 14a shows the variation of u (x component of the velocity) with y for $x = 0.5$, and Figure 14b shows the variation of v (y component of the velocity) with x for $y = 0.5$. Three grid sizes, 64×64, 128×128, and 256×256 are considered. The velocity profiles obtained on 128×128 grid compare well with the velocity profile obtained on 256×256 grid.

The generic implementation of the FSI solver is valid for non-unity cell aspect ratios $AR = \Delta_y/\Delta_x \neq 1$ as well. To test the validity, we compare the motion of soft solid on 128×128, 256×128, and 512×128 grids that have cell aspect ratios $AR = 1, 2$, and 4, respectively. Figure 15 compares the soft solid centroid trajectory for all the grids. For $AR = 2$ and 4, the centroid trajectory agrees well with the validated $AR = 1$ centroid trajectory.

The velocity distribution is smooth in both fluid and solid domains, with some sharp changes near the fluid–solid interface. We use the velocity distribution obtained on a 128×128 grid to elucidate this behavior. Figure 16 shows the velocity distributions along the centerlines ($x = 0.5$ and $y = 0.5$) of the cavity. The top row (Figure 16a–d) shows the variation of u with y and the bottom row (Figure 16e–h) shows the variation of v with x. Along with the instantaneous velocity profiles, the variation of ϕ is shown to represent the presence of solid on these centerlines. Due to the no-slip boundary conditions at the cavity walls, u is 0 at $y = 0$ and 1 at $y = 1$, and v is 0 at $x = 0$ and $x = 1$. In the region where $\phi = 0$ or $\phi = 1$, the velocity varies smoothly, while in the proximity of the fluid–solid interface ($0 < \phi < 1$), the velocity sometimes experiences sharp changes.

3.4 | Reversibility Test of a Circular Disk in Shear Flow

After releasing the stresses exerted on the hyperelastic solids, they generally return to their initial configuration [49]. The reversibility test examines this behavior by applying stress to the solid and releasing it. When describing solids on a Lagrangian grid, such

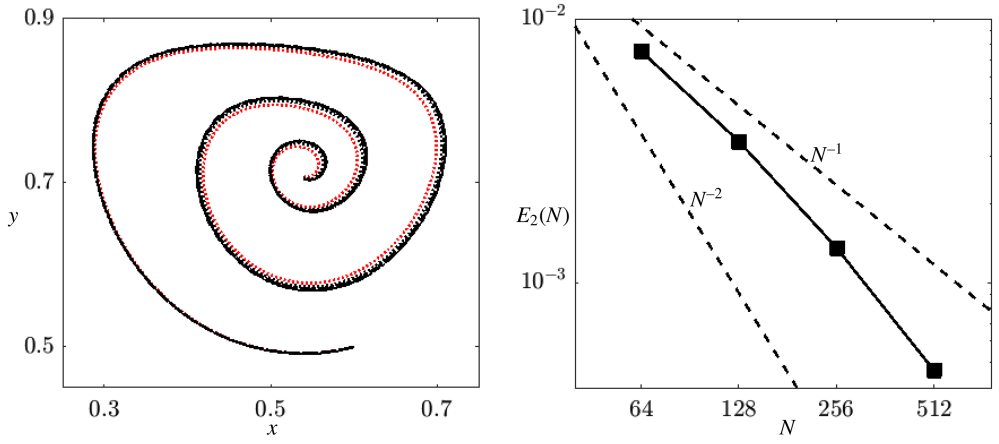

FIGURE 13 | (a) Soft solid centroid trajectory for $t \in [0, 20]$ and (b) L_2 error ($E_2(N)$) for various grid resolutions. In (a), ---- 64×64; ---- 128×128; - - - 256×256; - - - 512×512; —— 1024×1024. [Colour figure can be viewed at wileyonlinelibrary.com]

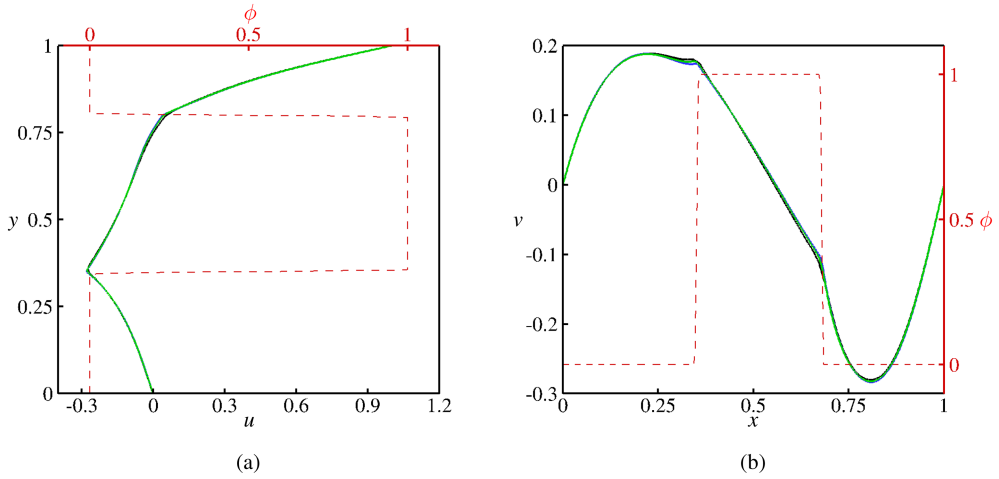

FIGURE 14 | Velocity distribution in a lid-driven cavity with a soft solid at $t = 8.20$ for different grid resolutions, at (a) $x = 0.5$ and (b) $y = 0.5$ locations. —— 64×64; —— 128×128; —— 256×256. The red dashed line (- - -) represents ϕ on a 256×256 grid. [Colour figure can be viewed at wileyonlinelibrary.com]

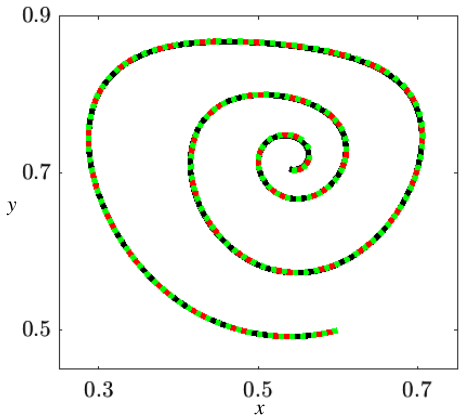

FIGURE 15 | Soft solid centroid trajectory for various cell aspect ratios (AR). —— $AR = 1$ (128×128); - - - $AR = 2$ (256×128); ····· $AR = 4$ (512×128). [Colour figure can be viewed at wileyonlinelibrary.com]

reversibility is readily satisfied as the grid tracks the movement of each node relative to their original configuration. However, reversibility is not trivial on a fixed Eulerian grid because the solid deformation is not explicitly traced through mesh motion. While using a VOF/PLIC procedure that exhibits discontinuities across the interface and cell boundaries, verifying the reversibility and stability is of utmost necessity. Otherwise, the strong spurious currents generated due to the stress imbalance might produce an oscillatory interface at equilibrium, resulting in inconsistencies between the initial and final configurations, and an unstable interface.

To perform a reversibility test and assess the accuracy of the solver while handling nonlinear hyperelastic materials, we consider the evolution of a Saint Venant-Kirchhoff circular disk in shear flow, similar to Ii et al. [10]. The computational domain size is $L_x \times L_y = 4 \times 4$ with domain extents $x \in [-L_x/2, L_x/2]$,

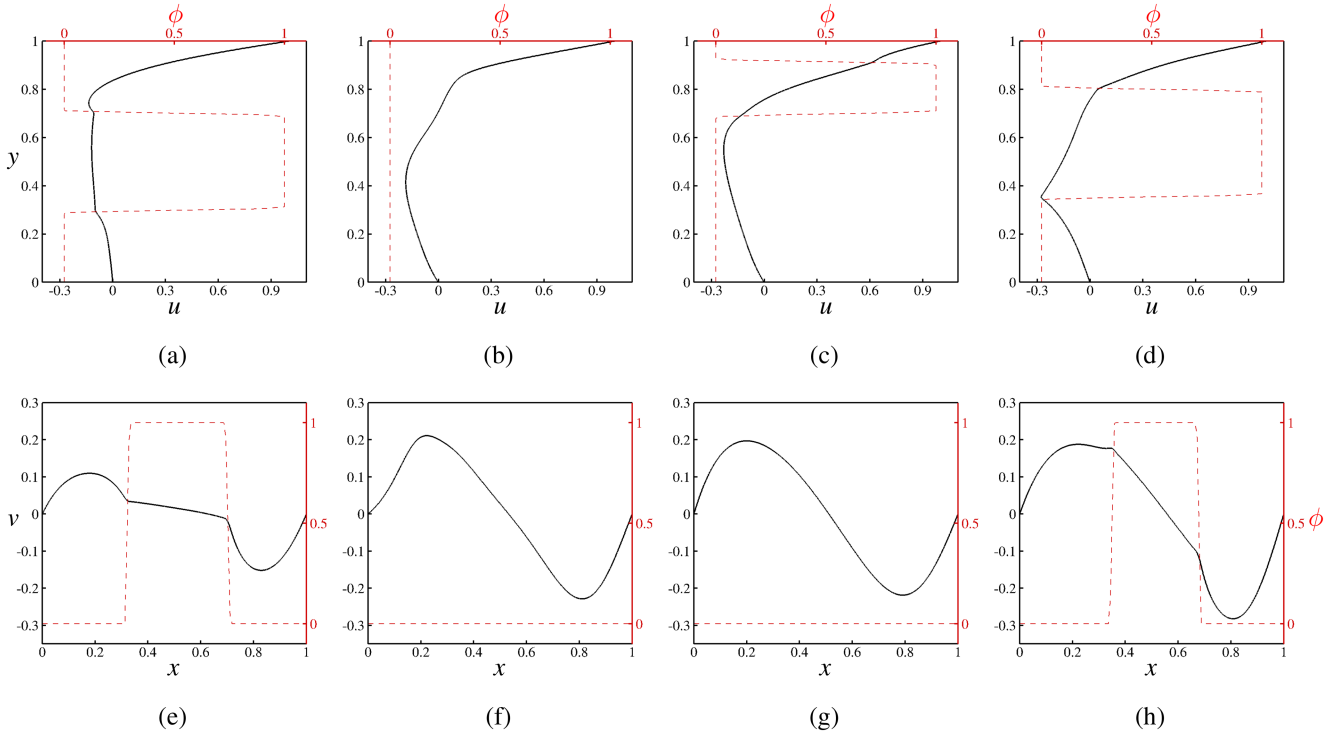

FIGURE 16 | Velocity distribution in a lid-driven cavity with a soft solid at (a–d) $x = 0.5$ and (e–h) $y = 0.5$ locations. (a, e) $t = 1.17$; (b, f) $t = 3.52$; (c, g) $t = 5.86$; (d, h) $t = 8.20$. The black line (——) represents velocity component and the red dashed line (- - -) represents ϕ. [Colour figure can be viewed at wileyonlinelibrary.com]

$y \in [-L_y/2, L_y/2]$, and the grid size is $N_x \times N_y = 256 \times 256$. Initially, the system is at rest and the unstressed circular solid disk is centered at $(x_c, y_c) = (0, 0)$ with diameter $d = 1$. The top and bottom walls start moving in opposite directions along the x axis with velocities V_w and $-V_w$, respectively. No-slip boundary conditions are imposed on the top and bottom walls, and periodicity is considered in the x direction. The solid is considered to be non-viscous ($\mu^s = 0$), and the fluid and solid densities are $\rho^f = \rho^s = 1$.

The problem parameters are determined according to the required shear rate $\dot{\gamma} = 2V_w/L_y$, Reynolds number $Re = \rho^f \dot{\gamma} d^2/\mu^f$, and the capillary number $Ca = \mu^f \dot{\gamma}/G^s$. We set $\dot{\gamma} = 1$ and $Re = 0.1$ by considering $V_w = 2$ and $\mu^f = 10$. We consider three values of Ca, $Ca = 0.1, 0.3, 0.5$, by varying $G^s = 100, 33.33, 20$.

The simulations are conducted for $t \in [0, 20]$, where the walls move in opposite directions for $t \in [0, 5]$ and stop moving after $t = 5$. For all three values of Ca, the disk reaches a steady state by $t = 5$, and the time taken to reach a steady state (referred to as the deformed steady state) increases with Ca. After the walls stop moving, far before $t = 20$, the disks return to their initial circular shape (referred to as the final steady state).

At the deformed steady state, the disk attains a smooth and stable elliptical shape without unwanted oscillations at the fluid–solid interface, and the disk shapes are in excellent agreement with the steady-state shapes reported by Ii et al. [10]. Figure 17 shows the current disk shape at $t = 5$ along with the results of Ii et al. [10]. The circular disk deforms to an elliptical shape whose major axis increases with Ca. The variation of the elliptical shape with Ca and the steady-state shapes are consistent with the results of Ii et al. [10]. Furthermore, the deformed steady state has a smooth interface without any wiggles at the fluid–solid interface, reflecting stability.

At the final steady state, the disk retains its initial smooth circular shape without unwanted oscillations at the fluid–solid interface. Figure 17 compares the final steady state with the initial state. The final state has a smooth interface without any wiggles on the solid surface. As a result, the initial and final configurations coincide very well.

To estimate the order of convergence, we compute the L_1 shape error at $t = 20$ for $Ca = 0.5$ on four different grids (32×32, 64×64, 128×128, 256×256). The L_1 shape error (E_1) is computed as

$$E_1(N = N_x) = \frac{1}{N_x N_y} \sum_{i=1}^{N_x} \sum_{j=1}^{N_y} \left| \phi_{i,j}(t = 20) - \phi_{i,j}(t = 0) \right|. \quad (47)$$

Figure 18 shows the variation of $E_1(N)$ with the grid size. The error decreases with grid size approximately as N^{-1} for higher grid resolutions.

3.5 | Sphere in a Lid-Driven Cavity

We consider the motion of a deformable neo-Hookean sphere in a 3D lid-driven cavity flow. The problem setup is similar to Valizadeh et al. [86] and Mao et al. [87]. The dimensions of the 3D cavity are $L_x \times L_y \times L_z = 1 \times 1 \times 1$, with no-slip boundary

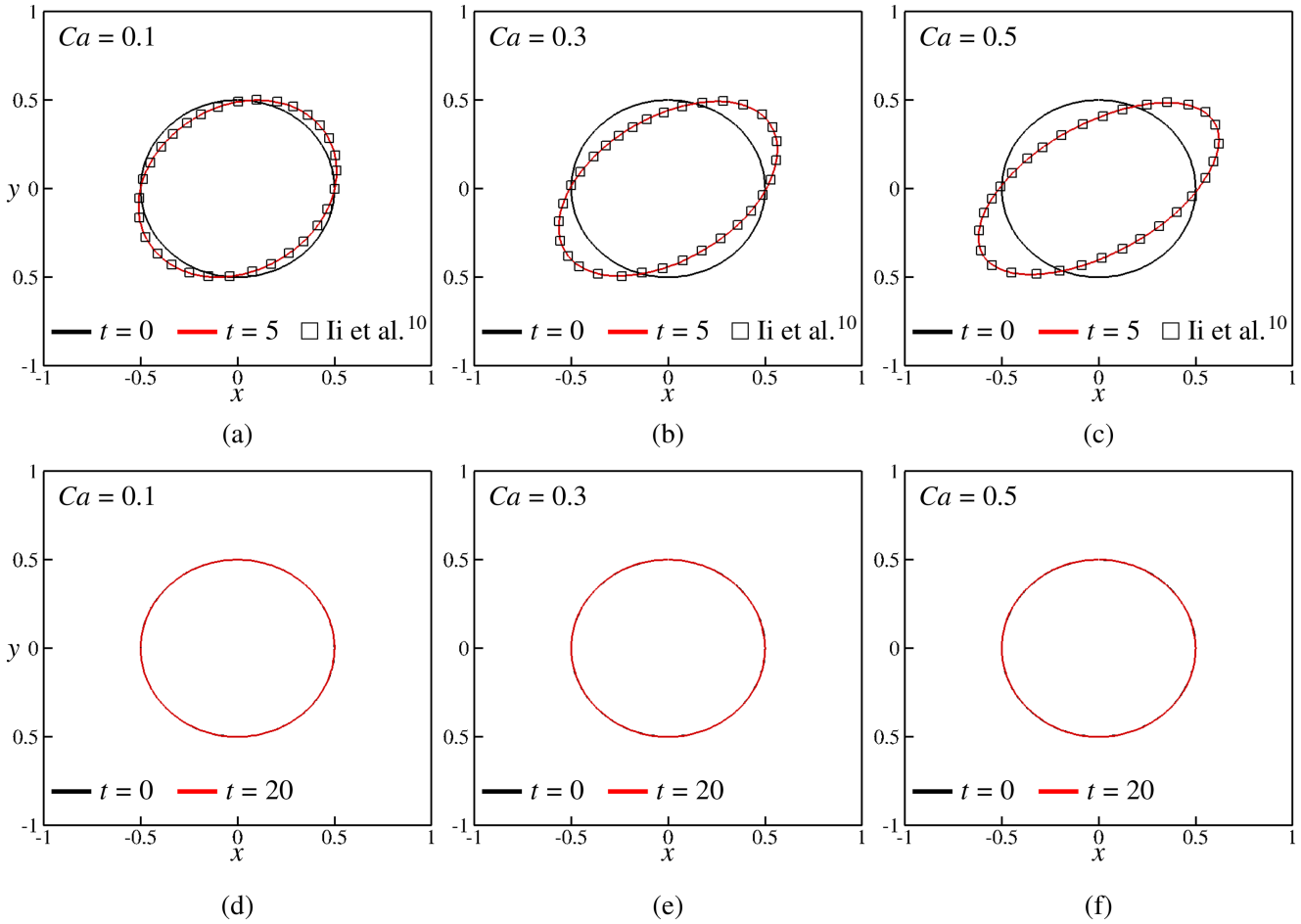

FIGURE 17 | Saint Venant-Kirchhoff circular disk in shear flow. [Colour figure can be viewed at wileyonlinelibrary.com]

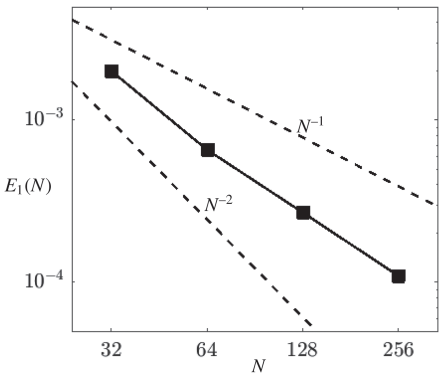

FIGURE 18 | L_1 shape error ($E_1(N)$) for Saint Venant-Kirchhoff circular disk in shear flow with $Ca = 0.5$.

conditions on the walls. Initially, the system is at rest, and the unstressed sphere is centered at $(x_c, y_c, z_c) = (0.6, 0.5, 0.5)$ with radius $r = 0.2$. The top wall ($y = L_y$) starts moving in the x direction with steady velocity $V_w = 1$, while the remaining walls stay stationary. The fluid properties are $\rho^f = 1$ and $\mu^f = 0.02$, and the solid properties are $\rho^s = 1$, $\mu^s = 0.02$, and $G^s = 0.5$. The grid size is $N_x \times N_y \times N_z = 64 \times 64 \times 64$ and we consider the motion for $t \in [0, 10]$.

The solid sphere moves in a clockwise direction due to the circulating flowfield generated by the moving top wall and it experiences high stretching near the top lid before it slides along the lid. Despite high stretching, the VOF/PLIC method-based FSI framework does not generate any unphysical solid fragments. Figure 19 shows the deformed solid and fluid flow in the 3D cavity at multiple time instants $t = 0, 1, 2, 3, 4, 5, 6, 7$. The solid initially moves towards the top wall and undergoes significant stretching due to high fluid stresses. However, the lubrication effect [88] between the solid and the wall prevents it from touching the top wall. As time proceeds and it approaches a settled state, its deformation and movement reduce. These observations are consistent with Valizadeh et al. [86].

To verify the results, we compute the 3D solid centroid trajectory as,

$$\boldsymbol{x}_c(t) = \frac{\sum_{i=1}^{N_x}\sum_{j=1}^{N_y}\sum_{k=1}^{N_z}\boldsymbol{x}_{i,j,k}\phi_{i,j,k}(t)\Delta_x\Delta_y\Delta_z}{\sum_{i=1}^{N_x}\sum_{j=1}^{N_y}\sum_{k=1}^{N_z}\phi_{i,j,k}(t)\Delta_x\Delta_y\Delta_z}. \tag{48}$$

Figure 20 shows the solid centroid trajectory in the $x - y$ plane for $t \in [0, 10]$. The solid centroid initially moves towards the top wall and spirals clockwise, consistent with the 3D snapshots.

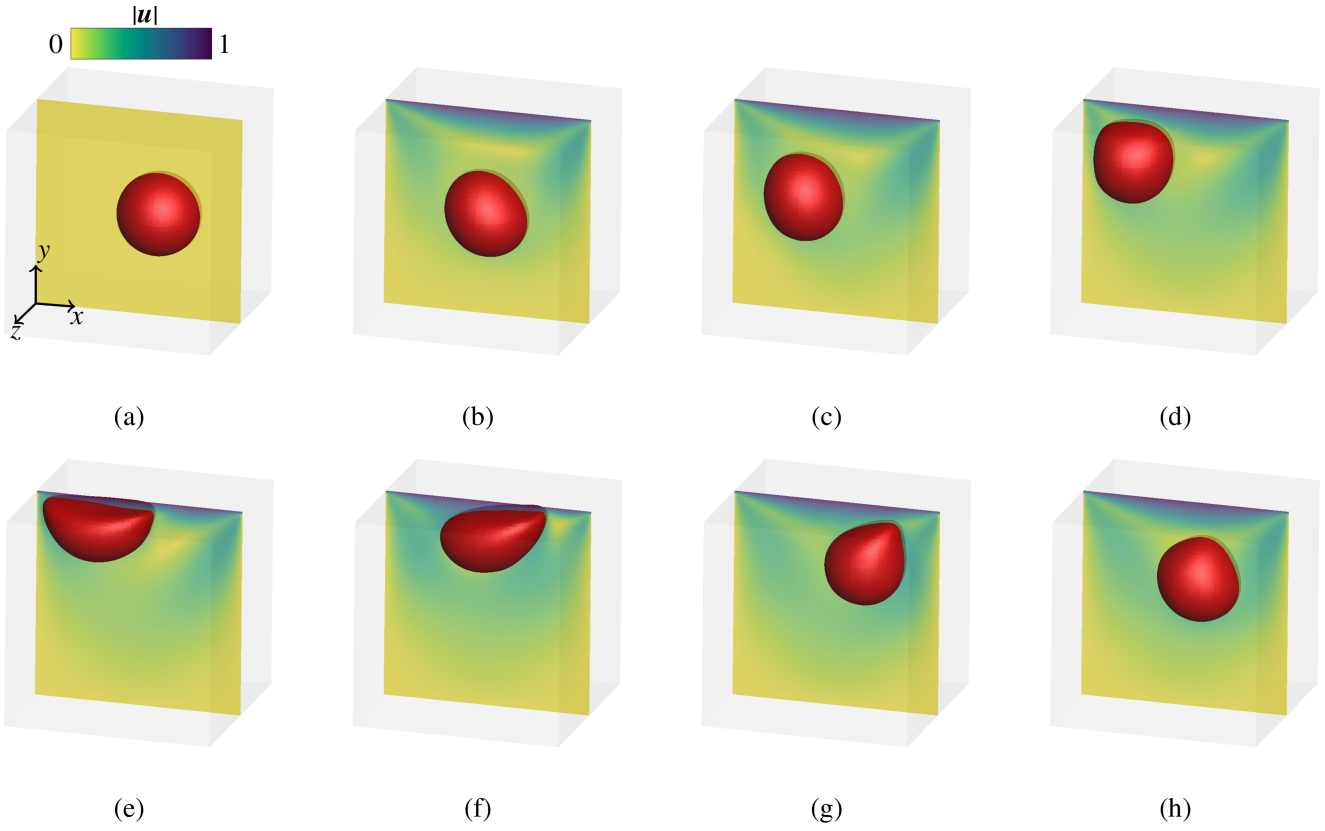

FIGURE 19 | 3D lid-driven cavity with a deformable sphere at different time instants (a–h) $t = 0, 1, 2, 3, 4, 5, 6, 7$. The vertical slice located at $z = 0.5$ shows flow speed contours and the red surface shows the solid shape ($\phi = 0.5$). [Colour figure can be viewed at wileyonlinelibrary.com]

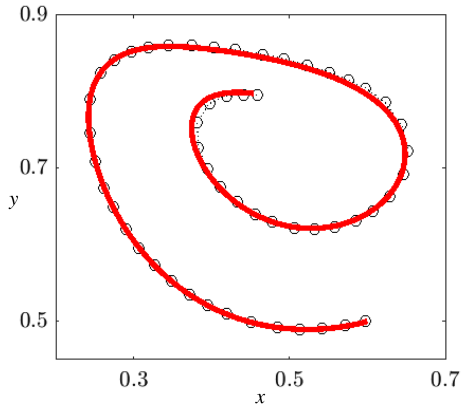

FIGURE 20 | Deformable sphere centroid trajectory in 3D lid-driven cavity for $t \in [0, 10]$. — VOF/PLIC ($64 \times 64 \times 64$); ○ Valizadeh et al. [86] ($h = 0.01$). [Colour figure can be viewed at wileyonlinelibrary.com]

Throughout the time history, the trajectory agrees well with that of Valizadeh et al. [86] obtained using PF modeling.

3.6 | DNS of Turbulent Channel Flow With a Deformable Compliant Wall

We use the FSI solver to perform DNS of turbulent channel flow with a neo-Hookean compliant bottom wall and a rigid top wall. The streamwise, spanwise, and wall-normal directions are along

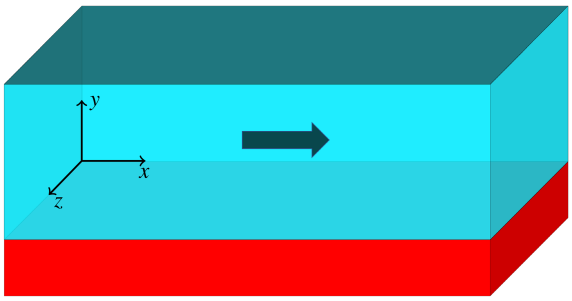

FIGURE 21 | Schematic of turbulent channel flow with a deformable compliant bottom wall and a rigid top wall. [Colour figure can be viewed at wileyonlinelibrary.com]

x, y, and z axes, respectively. Figure 21 shows a schematic of the problem. The domain size is $L_x \times L_y \times L_z = 2\pi\delta \times (2\delta + h^s) \times \pi\delta$, where δ is the half-height of the channel and h^s is the compliant wall thickness. The flow field is initialized with a statistically stationary turbulent channel flow developed over rigid walls, occupying $x \in [0, L_x]$, $y \in [0, 2\delta]$, $z \in [0, L_z]$ region, and the compliant wall has a flat interface initially with height h^s, occupying $x \in [0, L_x]$, $y \in [-h^s, 0)$, $z \in [0, L_z]$ region. We impose no-slip conditions on the top and bottom walls, and consider periodicity in streamwise and spanwise directions.

We consider a constant flow rate such that the bulk Reynolds number $Re_b = \rho^f U_b \delta / \mu^f$ is equal to 2800, where U_b is the fluid bulk velocity and the streamwise pressure gradient in the whole

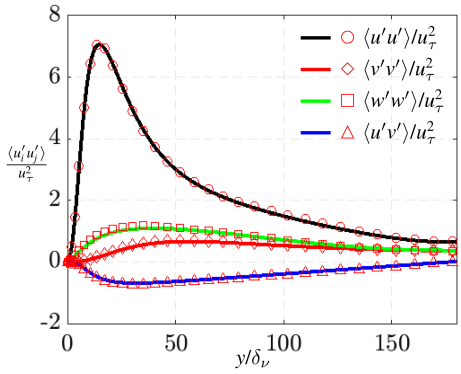

FIGURE 22 | Reynolds stress tensor components for turbulent channel flow with rigid top and bottom walls. Solid lines represent current results and symbols represent results of Moser et al. [89] for $Re_\tau \approx 180$. [Colour figure can be viewed at wileyonlinelibrary.com]

domain is adjusted to maintain constant U_b. For turbulent channel flow with rigid top and bottom walls, $Re_b = 2800$ corresponds to friction Reynolds number $Re_\tau = \rho^f u_\tau \delta / \mu^f \approx 180$, where $u_\tau = \sqrt{\tau_w / \rho^f}$ is the friction velocity and τ_w is the wall shear stress. To ensure two-way coupling, the parameters of the compliant wall are prescribed based on past works [2–4]. The parameters in the fluid domain are $\delta = 1$, $U_b = 1$, $\rho^f = 1$, $\mu^f = Re_b^{-1}$, and in the solid domain are $h^s = 0.5\delta = 0.5$, $\rho^s = 1$, $\mu^s = Re_b^{-1}$, $G^s = 0.5\rho^f U_b^2 = 0.5$.

The domain is discretized using uniform grid distribution in streamwise and spanwise directions. However, in the wall-normal direction, a non-uniform grid distribution is used in the fluid region away from the fluid–solid interface ($y \in (0.33, 2]$), while a uniform distribution is used close to the interface and in the solid domain ($y \in [-0.5, 0.33]$). The grid size is $N_x \times N_y \times N_z = 328 \times 312 \times 166$ and the grid resolution relative to the viscous length scale ($\delta_\nu = \mu^f / (\rho^f u_\tau)$) based on turbulent flow over rigid walls is $\Delta_x / \delta_\nu = 3.45$, $\Delta_z / \delta_\nu = 3.41$, and $\Delta_{y,min} / \delta_\nu = 0.79$.

We first simulate the turbulent channel flow with rigid top and bottom walls until it reaches a statistically stationary state. Then, we replace the rigid bottom wall with a deformable compliant wall, where we analyze the system's behavior after it passes the initial transient phase. To verify the validity of turbulent channel flow confined by rigid walls, we calculate Reynolds stress tensor defined as $\langle u_i' u_j' \rangle$, where $\langle \cdot \rangle$ represents spatio-temporal average (streamwise direction, spanwise direction, time) and $(\cdot)'$ represents fluctuating component in the Reynolds decomposition. Figure 22 compares the current Reynolds stresses at $Re_b = 2800$ ($Re_\tau \approx 180$) with that of Moser et al. [89] at $Re_\tau \approx 180$. The Reynolds stress components agree very well with the reference.

Figure 23 compares instantaneous visualizations of turbulent channel flow over rigid and compliant bottom walls. The vertical slices show streamwise velocity, and the red shade shows the bottom wall. For the channel with a rigid bottom wall, the turbulent flow near the top and bottom rigid walls is qualitatively similar, and the rigid bottom wall has a flat surface. As the flow develops over the compliant wall, the fluid stresses deform the compliant surface, and its dynamic motion affects the near-wall turbulence and modifies the flow. The wavy undulations of the compliant surface are significant enough to alter the near-wall turbulent flow. As a result, turbulent flow near the compliant surface is no longer qualitatively similar to the rigid top wall.

The VOF/PLIC-based fluid–solid interface remains sharp and stable throughout time history, and despite turbulent interactions, we do not observe numerical artifacts such as solid fragments. Figure 24 shows the contours of ϕ on a mid-spanwise plane for turbulent channel flow with a compliant bottom wall at $tU_b/\delta = 0$ and after the initial transient phase.

In past work involving such problems, fifth-order WENO scheme [3, 4] or LS [2] methods were used to capture the fluid–solid interface. The WENO procedure requires high grid resolution to reduce interface diffusion due to the diffusive nature of the scheme. The LS method requires a reinitialization procedure to maintain stability, which can be problem-dependent. However, as discussed above, the VOF/PLIC-based FSI method maintains interface stability and sharpness, bypassing the requirement of any problem-dependent stabilization procedure or large grids.

The wall compliance increases the Reynolds stress near the surface, and the shear stress component $\langle u'v' \rangle$ changes sign near the interface. Furthermore, the total shear stress follows a linear trend along the y axis, and in most of the compliant wall region, the contribution of hyperelastic stress is the highest. The total shear stress is calculated as $\tau^{total} = \tau^V + \tau^R + \tau^H$, where $\tau^V = (\rho/\mu)\partial\langle u \rangle / \partial y$ is the viscous stress contribution, $\tau^R = -\rho\langle u'v' \rangle$ is the Reynolds stress contribution, and $\tau^H = \rho G^s \langle \phi B_{xy} \rangle$ is the hyperelastic stress contribution. Figure 25a shows the components of the Reynolds stress tensor, and Figure 25b shows the total shear stress and its contributing components. The normal components ($\langle u'u' \rangle, \langle v'v' \rangle, \langle w'w' \rangle$) of the Reynolds stress tensor are the highest near the compliant surface (initially at $y = 0$). The shear stress component ($\langle u'v' \rangle$) of the Reynolds stress tensor changes sign in the vicinity of the compliant surface and has the highest magnitude close to the surface. The total shear stress follows a linear trend along the y axis, where its magnitude at the rigid support of the compliant wall ($y = -0.5$) is nearly double that at the rigid top wall ($y = 2$). Furthermore, in most of the compliant wall region, the contribution of hyperelastic stress (τ^H) is the highest. These observations are consistent with the numerical work of Esteghamatian et al. [2] that utilized the LS method to capture the interface.

The compliant surface exhibits spanwise aligned deformation patterns that propagate downstream, consistent with the past numerical [2, 3] and experimental [1] works. Figure 26a shows the wall-normal deformation of the compliant surface, and Figure 26b shows the pressure distribution on the compliant surface. The deformation pattern consists of spanwise aligned alternating troughs and crests in the streamwise direction. Also, the low and high pressures are associated with surface crests and troughs, respectively.

Inside the compliant wall, the spanwise vorticity suggests the surface motion resembles Rayleigh waves. Figure 27 shows the spanwise vorticity field near the fluid–solid interface on the mid-spanwise plane. Inside the solid, alternating positive and negative vortices are present, corresponding to the crest and

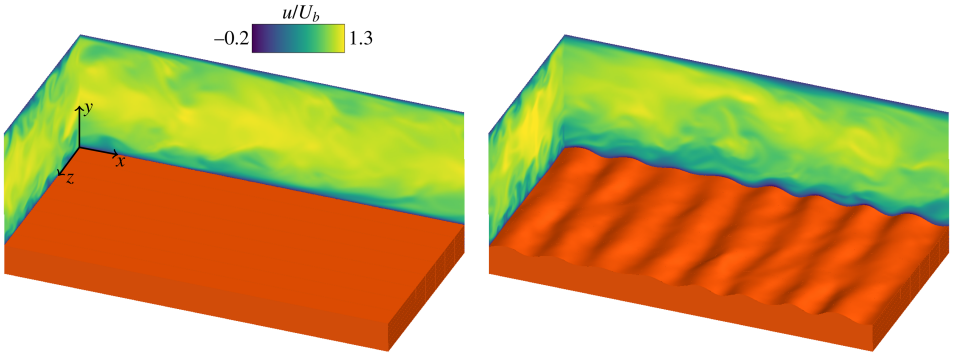

(a) (b)

FIGURE 23 | Turbulent channel flow with (a) rigid bottom wall and (b) compliant bottom wall at $Re_b = 2800$. Vertical slices show streamwise velocity contours and red shade shows the bottom wall. [Colour figure can be viewed at wileyonlinelibrary.com]

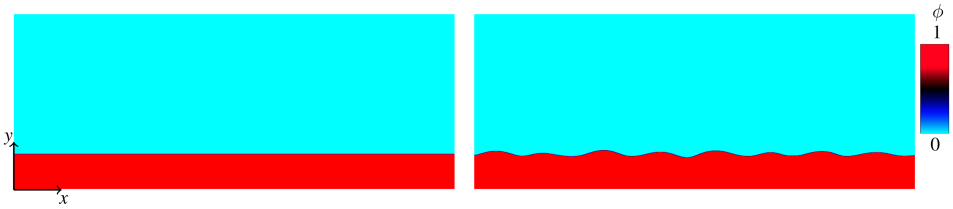

(a) (b)

FIGURE 24 | Contours of ϕ on mid-spanwise plane of turbulent channel flow with compliant bottom wall at (a) $tU_b/\delta = 0$ and (b) after the initial transient phase. [Colour figure can be viewed at wileyonlinelibrary.com]

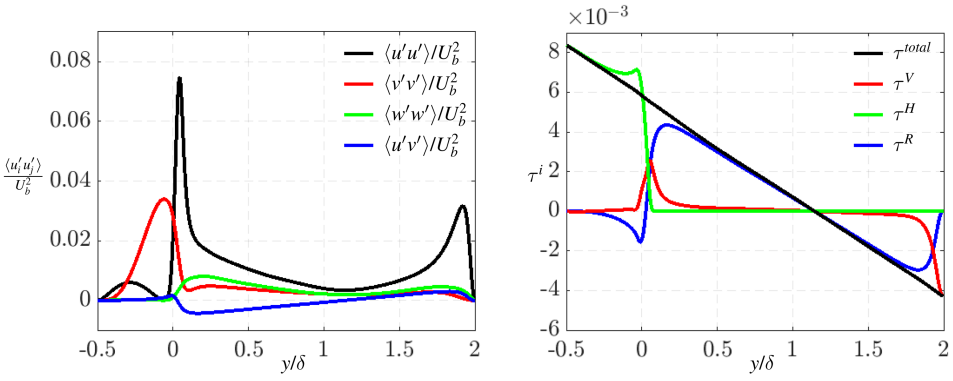

(a) (b)

FIGURE 25 | Stress distribution for turbulent channel flow with compliant bottom wall. (a) Reynolds stress tensor components and (b) the contribution of shear stress components to the total shear stress. [Colour figure can be viewed at wileyonlinelibrary.com]

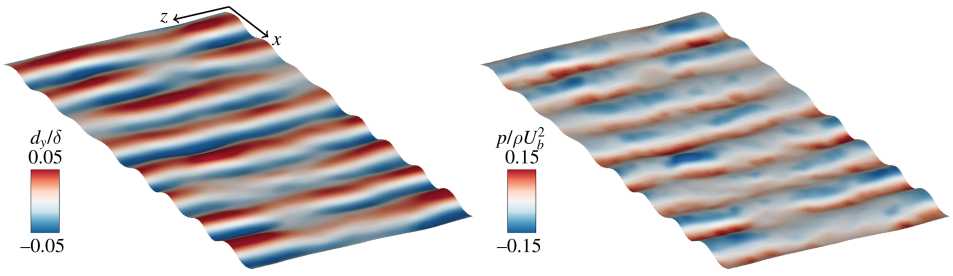

(a) (b)

FIGURE 26 | Deformed compliant surface colored with contours of (a) wall-normal deformation and (b) pressure distribution. [Colour figure can be viewed at wileyonlinelibrary.com]

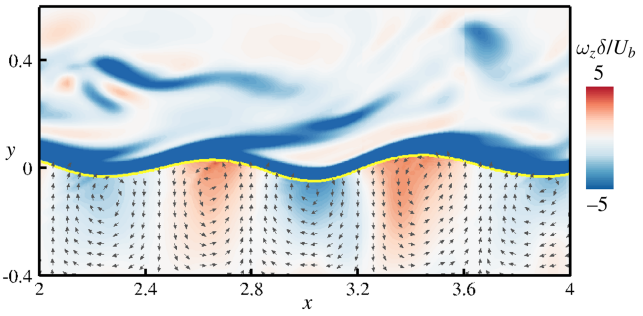

FIGURE 27 | Spanwise vorticity field near the compliant surface on the mid-spanwise plane. The yellow curve indicates the surface and the arrows inside the compliant wall show the velocity vectors. [Colour figure can be viewed at wileyonlinelibrary.com]

trough of the surface, respectively. It indicates the existence of counter-rotating spanwise rolls, and the velocity vectors verify it. This observation is also consistent with the numerical work of Esteghamatian et al. [2].

4 | Conclusions

We have developed a monolithic framework to simulate three-dimensional FSI problems involving incompressible flow and viscous hyperelastic solids on a fixed Cartesian grid. To simultaneously solve the governing equations of both fluid and solid subsystems, we use a one-continuum formulation, where the geometric VOF method [44] is used to track the fluid–solid interface. Here, the PLIC method [64–67] is used to reconstruct the interface, and the LE method [58, 61, 68] is used in the directionally split advection procedure. We consider linear and nonlinear Mooney–Rivlin materials [10, 49] to capture the hyperelastic mechanical behavior of the solid, where the left Cauchy–Green deformation tensor ($\boldsymbol{B}$) [49] accounts for the solid deformation. We use the fifth-order WENO-Z [50, 69] finite difference reconstruction procedure to treat the advection terms involved in the transport equation of $\boldsymbol{B}$ and a FVM [70] to solve the unified momentum conservation equations with incompressibility constraint. To the best of our knowledge, this is the first such 3D FSI framework developed using the geometric VOF (VOF/PLIC) IC method and applied to assess turbulent FSI interactions.

The performance of the Eulerian framework is evaluated using multiple benchmark problems [10, 42, 49, 83, 86, 87], and our results agree well with the results reported in the previous literature. Reversibility tests are conducted to verify that the hyperelastic solid returns to its initial state after the stresses are released, eliminating any concerns about the reversibility of the solid on an Eulerian grid. Furthermore, the generality of the implementation on grids with non-unity cell aspect ratios was also tested.

We have shown that the developed VOF/PLIC method-based framework maintains interface sharpness and stability throughout the time history. As a result, a high grid resolution is not required to compensate for interface diffusion, and no additional stabilization procedures are needed. The advantage of interface sharpness is demonstrated through one of the benchmark problems (circular disk in a lid-driven cavity), where our VOF/PLIC-based results on 128×128 grid agree well with the results of Sugiyama et al. [49] obtained on 1024×1024 Eulerian grid using the fifth-order WENO scheme to capture the interface.

Despite the discontinuity of the interface and stress jumps across the interface, the FSI framework does not generate unphysical solid fragments even when the solid undergoes significant deformation or is susceptible to pinching. Furthermore, no unwanted oscillations at the solid surface are present at steady states. These are typical concerns when using the VOF/PLIC method to capture interfaces of systems involving different materials/phases.

A DNS of turbulent channel flow with a deformable compliant bottom wall and a rigid top wall is performed, demonstrating the potential of the FSI framework to analyze complex turbulent interactions involving a wide range of length scales and time scales. The wall compliance increases the Reynolds stresses, and the compliant surface exhibits spanwise aligned deformation patterns that propagate downstream, consistent with past experimental and numerical works [1–3]. Inside the compliant wall, we verified the existence of counter-rotating spanwise rolls that suggest a similarity to Rayleigh wave motion, as observed in the numerical work of Esteghamatian et al. [2].

We have demonstrated that the geometric VOF-based FSI framework is robust in handling complex FSI problems involving turbulent interactions. Using such methods, one can bypass the requirements for high grid resolutions and stabilization procedures. Since solid shapes can be easily initialized using the VOF indicator function, one can use such a procedure to simulate the interaction of turbulent flows with complex geometries such as dynamic roughness elements and biofouling surface models.

Author Contributions

Soham Prajapati: writing – original draft preparation, review and editing, conceptualization, methodology, investigation. **Ali Fakhreddine:** writing – review and editing, conceptualization, methodology. **Krishnan Mahesh:** writing – review and editing, conceptualization, methodology, supervision.

Acknowledgments

This work was supported by the United States Office of Naval Research (ONR) under ONR Grants N00014-17-1-2676 and N00014-21-1-2455 with Dr. Ki-Han Kim and Dr. Yin Lu Young as grant monitors. The computational resources were provided by the U.S. Army Engineer Research and Development Center (ERDC) Department of Defense (DoD) Supercomputing Resource Center (DSRC) through the DoD High Performance Computing Modernization Program (HPCMP), the U.S. Navy DSRC through the DoD HPCMP, and the Minnesota Supercomputing Institute (MSI) at the University of Minnesota. The authors thank Dr. Karim Alamé and Marc Plasseraud for helpful discussions.

Funding

This work was supported by the United States Office of Naval Research (ONR) (Grant Nos. N00014-17-1-2676 and N00014-21-1-2455).

Conflicts of Interest

The authors declare no conflicts of interest.

Data Availability Statement

The data that support the findings of this study are available on request from the corresponding author. The data are not publicly available due to privacy or ethical restrictions.

References

1. J. Wang, S. S. Koley, and J. Katz, "On the Interaction of a Compliant Wall With a Turbulent Boundary Layer," *Journal of Fluid Mechanics* 899 (2020): A20.

2. A. Esteghamatian, J. Katz, and T. A. Zaki, "Spatiotemporal Characterization of Turbulent Channel Flow With a Hyperelastic Compliant Wall," *Journal of Fluid Mechanics* 942 (2022): A35.

3. M. E. Rosti and L. Brandt, "Numerical Simulation of Turbulent Channel Flow Over a Viscous Hyper-Elastic Wall," *Journal of Fluid Mechanics* 830 (2017): 708–735.

4. M. E. Rosti and L. Brandt, "Low Reynolds Number Turbulent Flows Over Elastic Walls," *Physics of Fluids* 32, no. 8 (2020): 083109, https://doi.org/10.1063/5.0018770.

5. I. K. Kaminaris and E. Balaras, "Direct Numerical Simulations of Turbulent Boundary Layers Developing Over Synthesised Calcareous Marine Biofouling Surfaces," *Ships and Offshore Structures* 21 (2024): 1–12.

6. J. Monty, E. Dogan, R. Hanson, A. Scardino, B. Ganapathisubramani, and N. Hutchins, "An Assessment of the Ship Drag Penalty Arising From Light Calcareous Tubeworm Fouling," *Biofouling* 32, no. 4 (2016): 451–464.

7. S. Sarakinos and A. Busse, "Investigation of Rough-Wall Turbulence Over Barnacle Roughness With Increasing Solidity Using Direct Numerical Simulations," *Physical Review Fluids* 7, no. 6 (2022): 064602.

8. Y. Liu and W. K. Liu, "Rheology of Red Blood Cell Aggregation by Computer Simulation," *Journal of Computational Physics* 220, no. 1 (2006): 139–154.

9. S. Ii, K. Sugiyama, S. Takagi, and Y. Matsumoto, "A Computational Blood Flow Analysis in a Capillary Vessel Including Multiple Red Blood Cells and Platelets," *Journal of Biomechanical Science and Engineering* 7, no. 1 (2012): 72–83.

10. S. Ii, K. Sugiyama, S. Takeuchi, S. Takagi, and Y. Matsumoto, "An Implicit Full Eulerian Method for the Fluid–Structure Interaction Problem," *International Journal for Numerical Methods in Fluids* 65, no. 1–3 (2011): 150–165.

11. K. Sugiyama, S. Ii, S. Takeuchi, S. Takagi, and Y. Matsumoto, "Full Eulerian Simulations of Biconcave Neo-Hookean Particles in a Poiseuille Flow," *Computational Mechanics* 46 (2010): 147–157.

12. S. S. Jain, K. Kamrin, and A. Mani, "A Conservative and Non-Dissipative Eulerian Formulation for the Simulation of Soft Solids in Fluids," *Journal of Computational Physics* 399 (2019): 108922.

13. H. H. Hu, N. A. Patankar, and M. Zhu, "Direct Numerical Simulations of Fluid–Solid Systems Using the Arbitrary Lagrangian–Eulerian Technique," *Journal of Computational Physics* 169, no. 2 (2001): 427–462.

14. C. W. Hirt, A. A. Amsden, and J. Cook, "An Arbitrary Lagrangian-Eulerian Computing Method for All Flow Speeds," *Journal of Computational Physics* 14, no. 3 (1974): 227–253.

15. C. Nitikitpaiboon and K. J. Bathe, "An Arbitrary Lagrangian–Eulerian Velocity Potential Formulation for Fluid-Structure Interaction," *Computers & Structures* 47, no. 4–5 (1993): 871–891.

16. T. J. Hughes, W. K. Liu, and T. K. Zimmermann, "Lagrangian–Eulerian Finite Element Formulation for Incompressible Viscous Flows," *Computer Methods in Applied Mechanics and Engineering* 29, no. 3 (1981): 329–349.

17. T. Tezduyar, M. Behr, and J. Liou, "A New Strategy for Finite Element Computations Involving Moving Boundaries and Interfaces—The Deforming-Spatial-Domain/Space-Time Procedure: I. The Concept and the Preliminary Numerical Tests," *Computer Methods in Applied Mechanics and Engineering* 94, no. 3 (1992): 339–351, https://doi.org/10.1016/0045-7825(92)90059-S.

18. T. E. Tezduyar, M. Behr, S. Mittal, and J. Liou, "A New Strategy for Finite Element Computations Involving Moving Boundaries and Interfaces—The Deforming-Spatial-Domain/Space-Time Procedure: II. Computation of Free-Surface Flows, Two-Liquid Flows, and Flows With Drifting Cylinders," *Computer Methods in Applied Mechanics and Engineering* 94, no. 3 (1992): 353–371.

19. T. J. Hughes and J. R. Stewart, "A Space-Time Formulation for Multiscale Phenomena," *Journal of Computational and Applied Mathematics* 74, no. 1–2 (1996): 217–229.

20. R. Torii, M. Oshima, T. Kobayashi, K. Takagi, and T. E. Tezduyar, "Influence of Wall Elasticity in Patient-Specific Hemodynamic Simulations," *Computers & Fluids* 36, no. 1 (2007): 160–168.

21. R. Torii, M. Oshima, T. Kobayashi, K. Takagi, and T. E. Tezduyar, "Fluid–Structure Interaction Modeling of a Patient-Specific Cerebral Aneurysm: Influence of Structural Modeling," *Computational Mechanics* 43 (2008): 151–159.

22. C. A. Taylor, T. J. Hughes, and C. K. Zarins, "Finite Element Modeling of Blood Flow in Arteries," *Computer Methods in Applied Mechanics and Engineering* 158, no. 1–2 (1998): 155–196.

23. A. Leuprecht, S. Kozerke, P. Boesiger, and K. Perktold, "Blood Flow in the Human Ascending Aorta: A Combined MRI and CFD Study," *Journal of Engineering Mathematics* 47 (2003): 387–404.

24. K. Stein, T. E. Tezduyar, S. Sathe, R. Benney, and R. Charles, "Fluid–Structure Interaction Modelling of Parachute Soft-Landing Dynamics," *International Journal for Numerical Methods in Fluids* 47, no. 6–7 (2005): 619–631.

25. K. Takizawa, S. Wright, C. Moorman, and T. E. Tezduyar, "Fluid–Structure Interaction Modeling of Parachute Clusters," *International Journal for Numerical Methods in Fluids* 65, no. 1–3 (2011): 286–307.

26. S. Mittal and T. E. Tezduyar, "Parallel Finite Element Simulation of 3D Incompressible Flows: Fluid-Structure Interactions," *International Journal for Numerical Methods in Fluids* 21, no. 10 (1995): 933–953.

27. K. Takizawa, B. Henicke, A. Puntel, T. Spielman, and T. E. Tezduyar, "Space-Time Computational Techniques for the Aerodynamics of Flapping Wings," *Journal of Applied Mechanics* 79, no. 1 (2011): 010903, https://doi.org/10.1115/1.4005073.

28. C. S. Peskin, "Flow Patterns Around Heart Valves: A Numerical Method," *Journal of Computational Physics* 10, no. 2 (1972): 252–271.

29. C. S. Peskin, "The Immersed Boundary Method," *Acta Numer* 11 (2002): 479–517.

30. R. Mittal and G. Iaccarino, "Immersed Boundary Methods," *Annual Review of Fluid Mechanics* 37 (2005): 239–261, https://doi.org/10.1146/annurev.fluid.37.061903.175743.

31. R. Glowinski, T. W. Pan, T. I. Hesla, D. D. Joseph, and J. Periaux, "A Distributed Lagrange Multiplier/Fictitious Domain Method for Flows Around Moving Rigid Bodies: Application to Particulate Flow," *International Journal for Numerical Methods in Fluids* 30, no. 8 (1999): 1043–1066.

32. R. Glowinski, T. W. Pan, T. I. Hesla, D. D. Joseph, and J. Periaux, "A Fictitious Domain Approach to the Direct Numerical Simulation of Incompressible Viscous Flow Past Moving Rigid Bodies: Application to Particulate Flow," *Journal of Computational Physics* 169, no. 2 (2001): 363–426.

33. Z. Yu, "A DLM/FD Method for Fluid/Flexible-Body Interactions," *Journal of Computational Physics* 207, no. 1 (2005): 1–27.

34. W. K. Liu, Y. Liu, D. Farrell, et al., "Immersed Finite Element Method and Its Applications to Biological Systems," *Computer Methods in Applied Mechanics and Engineering* 195, no. 13–16 (2006): 1722–1749.

35. L. T. Zhang and M. Gay, "Immersed Finite Element Method for Fluid-Structure Interactions," *Journal of Fluids and Structures* 23, no. 6 (2007): 839–857.

36. Z. Li and M. C. Lai, "The Immersed Interface Method for the Navier–Stokes Equations With Singular Forces," *Journal of Computational Physics* 171, no. 2 (2001): 822–842, https://doi.org/10.1006/jcph.2001.6813.

37. R. J. LeVeque and Z. Li, "The Immersed Interface Method for Elliptic Equations With Discontinuous Coefficients and Singular Sources," *SIAM Journal on Numerical Analysis* 31, no. 4 (1994): 1019–1044, https://doi.org/10.1137/0731054.

38. S. Wang, "From Immersed Boundary Method to Immersed Continuum Methods," *International Journal for Multiscale Computational Engineering* 4, no. 1 (2006): 127–146, https://doi.org/10.1615/IntJMultCompEng.v4.i1.90.

39. C. D. Eggleton and A. S. Popel, "Large Deformation of Red Blood Cell Ghosts in a Simple Shear Flow," *Physics of Fluids* 10, no. 8 (1998): 1834–1845.

40. X. Gong, K. Sugiyama, S. Takagi, and Y. Matsumoto, "The Deformation Behavior of Multiple Red Blood Cells in a Capillary Vessel," (2009).

41. C. Kadapa, W. Dettmer, and D. Perić, "A Fictitious Domain/Distributed Lagrange Multiplier Based Fluid–Structure Interaction Scheme With Hierarchical B-Spline Grids," *Computer Methods in Applied Mechanics and Engineering* 301 (2016): 1–27.

42. H. Zhao, J. B. Freund, and R. D. Moser, "A Fixed-Mesh Method for Incompressible Flow–Structure Systems With Finite Solid Deformations," *Journal of Computational Physics* 227, no. 6 (2008): 3114–3140.

43. G. Tryggvason, R. Scardovelli, and S. Zaleski, *Direct Numerical Simulations of Gas–Liquid Multiphase Flows* (Cambridge University Press, 2011).

44. C. W. Hirt and B. D. Nichols, "Volume of Fluid (VOF) Method for the Dynamics of Free Boundaries," *Journal of Computational Physics* 39, no. 1 (1981): 201–225.

45. S. Osher and J. A. Sethian, "Fronts Propagating With Curvature-Dependent Speed: Algorithms Based on Hamilton-Jacobi Formulations," *Journal of Computational Physics* 79, no. 1 (1988): 12–49.

46. D. Jacqmin, "Calculation of Two-Phase Navier-Stokes Flows Using Phase-Field Modeling," *Journal of Computational Physics* 155, no. 1 (1999): 96–127.

47. N. Nagano, K. Sugiyama, S. Takeuchi, II, S. Takagi, and Y. Matsumoto, "Full-Eulerian Finite-Difference Simulation of Fluid Flow in Hyperelastic Wavy Channel," *Journal of Fluid Science and Technology* 5, no. 3 (2010): 475–490.

48. S. Shin, J. Chergui, and D. Juric, "Interaction of a Deformable Solid With Two-Phase Flows: An Eulerian-Based Numerical Model for Fluid–Structure Interaction Using the Level Contour Reconstruction Method," *International Journal for Numerical Methods in Fluids* 92, no. 11 (2020): 1478–1505.

49. K. Sugiyama, S. Ii, S. Takeuchi, S. Takagi, and Y. Matsumoto, "A Full Eulerian Finite Difference Approach for Solving Fluid–Structure Coupling Problems," *Journal of Computational Physics* 230, no. 3 (2011): 596–627.

50. G. S. Jiang and C. W. Shu, "Efficient Implementation of Weighted ENO Schemes," *Journal of Computational Physics* 126, no. 1 (1996): 202–228.

51. F. Xiao, Y. Honma, and T. Kono, "A Simple Algebraic Interface Capturing Scheme Using Hyperbolic Tangent Function," *International Journal for Numerical Methods in Fluids* 48, no. 9 (2005): 1023–1040.

52. K. Yokoi, "Efficient Implementation of THINC Scheme: A Simple and Practical Smoothed VOF Algorithm," *Journal of Computational Physics* 226, no. 2 (2007): 1985–2002.

53. S. Ii, K. Sugiyama, S. Takeuchi, S. Takagi, Y. Matsumoto, and F. Xiao, "An Interface Capturing Method With a Continuous Function: The THINC Method With Multi-Dimensional Reconstruction," *Journal of Computational Physics* 231, no. 5 (2012): 2328–2358.

54. H. Esmailzadeh and M. Passandideh-Fard, "Numerical and Experimental Analysis of the Fluid-Structure Interaction in Presence of a Hyperelastic Body," *Journal of Fluids Engineering* 136, no. 11 (2014): 111107.

55. B. Valkov, C. H. Rycroft, and K. Kamrin, "Eulerian Method for Multiphase Interactions of Soft Solid Bodies in Fluids," *Journal of Applied Mechanics* 82, no. 4 (2015): 041011.

56. S. Prajapati, S. Anantharamu, and K. Mahesh, "Direct Numerical Simulation-Based Vibroacoustic Response of Plates Excited by Turbulent Wall-Pressure Fluctuations," *Journal of Fluid Mechanics* 976 (2023): A2.

57. S. Anantharamu and K. Mahesh, "Response of a Plate in Turbulent Channel Flow: Analysis of Fluid–Solid Coupling," *Journal of Fluids and Structures* 100 (2021): 103173, https://doi.org/10.1016/j.jfluidstructs.2020.103173.

58. D. Gueyffier, J. Li, A. Nadim, R. Scardovelli, and S. Zaleski, "Volume-Of-Fluid Interface Tracking With Smoothed Surface Stress Methods for Three-Dimensional Flows," *Journal of Computational Physics* 152, no. 2 (1999): 423–456.

59. E. Aulisa, S. Manservisi, R. Scardovelli, and S. Zaleski, "Interface Reconstruction With Least-Squares Fit and Split Advection in Three-Dimensional Cartesian Geometry," *Journal of Computational Physics* 225, no. 2 (2007): 2301–2319.

60. G. D. Weymouth and D. K. P. Yue, "Conservative Volume-Of-Fluid Method for Free-Surface Simulations on Cartesian-Grids," *Journal of Computational Physics* 229, no. 8 (2010): 2853–2865.

61. R. Scardovelli and S. Zaleski, "Interface Reconstruction With Least-Square Fit and Split Eulerian–Lagrangian Advection," *International Journal for Numerical Methods in Fluids* 41, no. 3 (2003): 251–274.

62. A. Baraldi, M. Dodd, and A. Ferrante, "A Mass-Conserving Volume-Of-Fluid Method: Volume Tracking and Droplet Surface-Tension in Incompressible Isotropic Turbulence," *Computers & Fluids* 96 (2014): 322–337.

63. T. Arrufat, M. Crialesi-Esposito, D. Fuster, et al., "A Mass-Momentum Consistent, Volume-Of-Fluid Method for Incompressible Flow on Staggered Grids," *Computers & Fluids* 215 (2021): 104785.

64. R. B. DeBar, *Fundamentals of the KRAKEN Code* (Lawrence Livermore National Lab.(LLNL), 1974).

65. D. L. Youngs, "Time-Dependent Multi-Material Flow With Large Fluid Distortion," *Numerical Methods for Fluid Dynamics* (1982).

66. D. L. Youngs, "An Interface Tracking Method for a 3D Eulerian Hydrodynamics Code," *Atomic Weapons Research Establishment (AWRE) Technical Report* 44, no. 92 (1984): 35.

67. J. Li, "Calcul d'interface affine par morceaux," *Comptes Rendus de L'académie Des Sciences. Série II, Mécanique, Physique, Chimie, Astronomie* 320, no. 8 (1995): 391–396.

68. K. Alamé, "Numerical Prediction Of Drag Reduction and Interfacial Shapes Over Superhydrophobic Surfaces," (2020), PhD thesis, University of Minnesota.

69. R. Borges, M. Carmona, B. Costa, and W. S. Don, "An Improved Weighted Essentially Non-Oscillatory Scheme for Hyperbolic Conservation Laws," *Journal of Computational Physics* 227, no. 6 (2008): 3191–3211.

70. K. Mahesh, G. Constantinescu, and P. Moin, "A Numerical Method for Large-Eddy Simulation in Complex Geometries," *Journal of Computational Physics* 197, no. 1 (2004): 215–240.

71. G. Tryggvason, M. Sussman, and M. Hussaini, "Immersed Boundary Methods for Fluid Interfaces," in *Computational Methods for Multiphase Flow* (Cambridge University Press, 2007), 37–77.

72. M. Mooney, "A Theory of Large Elastic Deformation," *Journal of Applied Physics* 11, no. 9 (1940): 582–592.

73. R. S. Rivlin, "Large Elastic Deformations of Isotropic Materials IV. Further Developments of the General Theory," *Philosophical Transactions of the Royal Society of London. Series A, Mathematical and Physical Sciences* 241, no. 835 (1948): 379–397.

74. J. Bonet and R. D. Wood, *Nonlinear Continuum Mechanics for Finite Element Analysis* (Cambridge University Press, 1997).

75. Y. Li, K. Alame, and K. Mahesh, "Feature-Resolved Computational and Analytical Study of Laminar Drag Reduction by Superhydrophobic Surfaces," *Physical Review Fluids* 2, no. 5 (2017): 054002.

76. K. Alamé and K. Mahesh, "Wall-Bounded Flow Over a Realistically Rough Superhydrophobic Surface," *Journal of Fluid Mechanics* 873 (2019): 977–1019.

77. R. Ma, K. Alamé, and K. Mahesh, "Direct Numerical Simulation of Turbulent Channel Flow Over Random Rough Surfaces," *Journal of Fluid Mechanics* 908 (2021): A40.

78. R. Ma and K. Mahesh, "Global Stability Analysis and Direct Numerical Simulation of Boundary Layers With an Isolated Roughness Element," *Journal of Fluid Mechanics* 949 (2022): A12.

79. R. Ma and K. Mahesh, "Boundary Layer Transition due to Distributed Roughness: Effect of Roughness Spacing," *Journal of Fluid Mechanics* 977 (2023): A27.

80. S. Anantharamu and K. Mahesh, "Analysis of Wall-Pressure Fluctuation Sources From Direct Numerical Simulation of Turbulent Channel Flow," *Journal of Fluid Mechanics* 898 (2020): 898, https://doi.org/10.1017/jfm.2020.412.

81. R. Scardovelli and S. Zaleski, "Analytical Relations Connecting Linear Interfaces and Volume Fractions in Rectangular Grids," *Journal of Computational Physics* 164, no. 1 (2000): 228–237.

82. S. Pawar and O. San, "CFD Julia: A Learning Module Structuring an Introductory Course on Computational Fluid Dynamics," *Fluids* 4, no. 3 (2019): 159.

83. S. T. Zalesak, "Fully Multidimensional Flux-Corrected Transport Algorithms for Fluids," *Journal of Computational Physics* 31, no. 3 (1979): 335–362.

84. X. Wang and L. T. Zhang, "Interpolation Functions in the Immersed Boundary and Finite Element Methods," *Computational Mechanics* 45 (2010): 321–334.

85. T. Dunne, "An Eulerian Approach to Fluid–Structure Interaction and Goal-Oriented Mesh Adaptation," *International Journal for Numerical Methods in Fluids* 51, no. 9–10 (2006): 1017–1039.

86. N. Valizadeh, X. Zhuang, and T. Rabczuk, "A Monolithic Finite Element Method for Phase-Field Modeling of Fully Eulerian Fluid–Structure Interaction," *Computer Methods in Applied Mechanics and Engineering* 435 (2025): 117618.

87. X. Mao, B. Rath, and R. Jaiman, "A 3D Phase-Field Based Eulerian Variational Framework for Multiphase Fluid–Structure Interaction With Contact Dynamics," *Computer Methods in Applied Mechanics and Engineering* 429 (2024): 117172.

88. J. M. Skotheim and L. Mahadevan, "Soft Lubrication: The Elastohydrodynamics of Nonconforming and Conforming Contacts," *Physics of Fluids* 17, no. 9 (2005): 092101, https://doi.org/10.1063/1.1985467.

89. R. D. Moser, J. Kim, and N. N. Mansour, "Direct Numerical Simulation of Turbulent Channel Flow up to Re$\tau = 590$," *Physics of Fluids* 11, no. 4 (1999): 943–945.